Evidence for rapid weathering response to climatic warming during the Toarcian Oceanic Anoxic Event

Theodore R. Them II[1,2*], Benjamin C. Gill[1], David Selby[3], Darren R. Gröcke[3], Richard M. Friedman[4], and Jeremy D. Owens[2]

[1]*Department of Geosciences, Virginia Polytechnic Institute and State University, Blacksburg, Virginia 24061, USA*

[2]*Department of Earth, Ocean and Atmospheric Science & National High Magnetic Field Laboratory, Florida State University, Tallahassee, Florida 32306, USA*

[3]*Department of Earth Sciences, Durham University, Durham, DH1 3LE, UK*

[4]*Pacific Centre for Isotopic and Geochemical Research, Department of Earth, Ocean and Atmospheric Sciences, University of British Columbia, Vancouver, V6T 1Z4, Canada*

**Email: tthem@fsu.edu*

Chemical weathering consumes atmospheric carbon dioxide through the breakdown of silicate minerals and is thought to stabilize Earth's long-term climate. However, the potential influence of silicate weathering on atmospheric pCO_2 levels on geologically short timescales (10^3 – 10^5 years) remains poorly constrained. Here we focus on the record of a transient interval of severe climatic warming across the Toarcian Oceanic Anoxic Event or T-OAE from an open ocean sedimentary succession from western North America. Paired osmium isotope data and numerical modelling results suggest that weathering rates may have increased by 215% and potentially up to 530% compared to the pre-event baseline,

which would have resulted in the sequestration of significant amounts of atmospheric CO_2. This process would have also led to increased delivery of nutrients to the oceans and lakes stimulating bioproductivity and leading to the subsequent development of shallow-water anoxia, the hallmark of the T-OAE. This enhanced bioproductivity and anoxia would have resulted in elevated rates of organic matter burial that would have acted as an additional negative feedback on atmospheric pCO_2 levels. Therefore, the enhanced weathering modulated by initially increased pCO_2 levels would have operated as both a direct and indirect negative feedback to end the T-OAE.

The chemical weathering of rocks constitutes a negative and stabilizing feedback to Earth's long-term (10^8 – 10^9 yr) climate by consuming atmospheric CO_2, modulating the greenhouse effect and, in turn, global temperatures[1,2,3]. On these timescales, chemical weathering is dominantly regulated by tectonics, atmospheric pCO_2, temperature, the lithology of materials being weathered, and the strength of the hydrological cycle[3]. Although the influence of weathering on long-term climate is well established[3], much less is known about how this process potentially operates and influences climate on shorter times scales ($<10^6$ yr)[4].

The T-OAE of the Early Jurassic Period constituted an ephemeral interval of global warming, perturbations in the global carbon cycle[5], widespread oceanic anoxia[6], and elevated marine extinction rates[7]. These environmental and ecological changes have been linked to the emplacement of the Karoo-Ferrar Large Igneous Province (LIP) and subsequent injection of greenhouse gases into the atmosphere[8] (Fig. 1). Specifically, the addition of mantle-derived CO_2 and thermogenic CH_4 derived from the emplacement of the LIP[9,10,11] and subsequent releases of CH_4 from marine clathrates[12,13] and terrestrial environments[14,15] to the oceans and atmosphere are the proposed drivers of the T-OAE warming and carbon cycle perturbations. These perturbations

are now recorded in sedimentary successions as pronounced negative carbon isotope excursions (CIEs), which occurred during a long-term trend to more positive carbon isotope values. This negative excursion is followed by a positive CIE thought to be the result of enhanced organic matter burial under anoxic conditions in marine and lacustrine environments[5,6]. Collectively, these two carbon isotope excursions are used to stratigraphically define the T-OAE interval.

Under the enhanced greenhouse effect triggered by elevated levels of atmospheric greenhouse gases during the T-OAE, global temperatures would have increased and the hydrological cycle would have strengthened[5]. Rising pCO_2, global temperatures, and precipitation rates would have led to accelerated weathering rates[3]. To investigate the proposition of accelerated weathering during the T-OAE, we have utilized osmium isotope ($^{187}Os/^{188}Os$) stratigraphy to reconstruct the $^{187}Os/^{188}Os$ composition of seawater over the event (see Supplemental Information).

The $^{187}Os/^{188}Os$ composition of seawater ($^{187}Os/^{188}Os_{sw}$) reflects the sources of osmium to the ocean: rivers that drain continents ($^{187}Os/^{188}Os_{cont} \approx 1.4$) and aeolian dust ($^{187}Os/^{188}Os_{aeol} \approx 1.04$) represent a radiogenic end-member, and alteration of juvenile ocean crust or from the mantle ($^{187}Os/^{188}Os_{m} \approx 0.12$) and cosmic dust/bolides ($^{187}Os/^{188}Os_{cos} \approx 0.12$) represent an unradiogenic end-member[16] (SI Fig. 1 and Supplemental Information). The flux of cosmic and aeolian dust represents a small fraction of the global input of osmium to the oceans and does not readily dissolve in seawater, and therefore does not appreciably affect the ocean's $^{187}Os/^{188}Os_{sw}$ composition[16,17]. The present-day $^{187}Os/^{188}Os_{sw}$ (~1.06) reflects the relatively greater input of continental-derived osmium to the ocean as compared to mantle-sourced osmium. Importantly, the short residence time of osmium in the oceans (~10^3-10^4 yr)[18] permits the osmium isotope system to record ephemeral changes in global weathering patterns on the order of 10^3 to 10^5

years in the geological record[19].

The $^{187}Os/^{188}Os$ compositions of organic-rich sediments are known to record the $^{187}Os/^{188}Os$ composition of contemporaneous seawater[19], and serve as an archive of the past marine osmium isotope compositions. A previous osmium isotope study of the T-OAE interval from a sedimentary succession in the Cleveland Basin of Yorkshire, United Kingdom indicates that, during the event, there was a concomitant, transient increase of $^{187}Os/^{188}Os_{sw}$ values by 0.7[20] (Fig. 2). This record was originally interpreted to be the result of an increase in continental weathering rates of 400 to 800%[20]. However, it has been suggested that these data reflect regional climatic changes where enhanced local runoff influenced the $^{187}Os/^{188}Os_{sw}$ composition of the European epicontinental sea, which the Cleveland Basin was part of (Fig. 1), and therefore the $^{187}Os/^{188}Os$ record does not reflect a global weathering signal[21]. Key to this dispute is whether the Cleveland Basin was significantly hydrographically restricted so the local $^{187}Os/^{188}Os_{sw}$ signal could be modified[21,22]. A recently published osmium isotope record across the T-OAE from the Mochras borehole[23], located in nearby Wales, displays a much less pronounced excursion of 0.4 during the T-OAE interval (Fig. 2), which further suggests that geochemical changes recorded in the Cleveland Basin were likely influenced by regional climatic and oceanographic dynamics[18,24,25].

To resolve whether the transient increases in $^{187}Os/^{188}Os$ observed across the T-OAE were indeed a global signal, we have investigated the osmium isotope record from the Lower Jurassic Fernie Formation of the Western Canada Sedimentary Basin located in present-day western Alberta (Fig. 1). This new location was situated on the eastern margin of the ocean of Panthalassa and therefore was located in a different ocean basin from the previously studied Yorkshire and Mochras sites (Figs 1 and 2). Ammonite biostratigraphy and carbon isotope

stratigraphy of the Fernie Formation at East Tributary of Bighorn Creek has identified the upper Pliensbachian to middle Toarcian interval and the T-OAE CIEs[15,26,27,28]. Zircon U-Pb dates from two bentonites located near the base of the section also provide temporal constraint and an age model for the section (Fig. 3; see Methods and Supplementary Data). Importantly, the entire interval of the East Tributary succession contains organic-rich strata (2-8% TOC; Figs 1 and 3)[15], and thus represents an ideal location to reconstruct the global $^{187}Os/^{188}Os_{sw}$ over the T-OAE interval (see Supplemental Information).

Results

$^{187}Os/^{188}Os_i$ record from North America

The high-resolution initial $^{187}Os/^{188}Os$ ($^{187}Os/^{188}Os_i$) record of the East Tributary succession (see Supplemental Information) displays extremely unradiogenic values ($^{187}Os/^{188}Os_i \approx 0.25$) in the Pliensbachian and Lowest Toarcian, followed by a prominent radiogenic excursion ($^{187}Os/^{188}Os_i \approx 0.6$) during the Toarcian CIEs (Fig. 3). The $^{187}Os/^{188}Os_i$ values decrease after the Toarcian CIE and asymptotically approach ~0.4 (Fig. 3; see Supplemental Information). Locally at East Tributary, aluminum and titanium concentrations increase 3-fold during the $^{187}Os/^{188}Os_i$ excursion and remain high for the rest of the record (see Fig. 3 and SI Dataset 1), which suggests a local increase in the contribution of continentally derived materials during the event. However, their concentrations remain high as $^{187}Os/^{188}Os_i$ values decrease after the Toarcian CIE, which suggests a minimal influence of a detrital component of rhenium and osmium to the osmium isotopic signature (see Fig. 3, Methods, and SI Dataset 1).

Discussion

Comparison of Early Jurassic $^{187}Os/^{188}Os_i$ records

Other marine $^{187}Os/^{188}Os_i$ records from the Lower Jurassic (Hettangian through Toarcian stages) generally show unradiogenic values[20,23,29,30]. These are likely related to relatively elevated inputs of unradiogenic osmium from the weathering of the Central Atlantic Magmatic Province (CAMP) and the alteration of juvenile oceanic lithosphere or direct injection of mantle-derived osmium from initial opening of the North Atlantic[31]. The Upper Pliensbachian portion of our record from northeastern Panthalassa has broadly similar values to those observed in the European epicontinental sea[20,23,29], which suggests they are representative of the global $^{187}Os/^{188}Os_{sw}$ values, and indicative of a well-mixed Early Jurassic ocean. Further, the East Tributary $^{187}Os/^{188}Os_i$ record shows a similar pattern to the other available records during the interval that contains the T-OAE[20,23]. All the sites record an excursion to higher $^{187}Os/^{188}Os_i$ values that follow the falling limb of the Toarcian negative CIE. This trend is followed by a return to lower $^{187}Os/^{188}Os_i$ values after the rising limb of the negative CIE. However, in all cases $^{187}Os/^{188}Os_i$ declines to values slightly higher than those observed before the excursion.

While all the $^{187}Os/^{188}Os_i$ records display a similar overall pattern, their $^{187}Os/^{188}Os_i$ values differ. The Yorkshire and East Tributary datasets have similar $^{187}Os/^{188}Os_i$ values before and after the T-OAE (~0.3 and ~0.4, respectively); however, the Yorkshire dataset shows an excursion to significantly more radiogenic values ($^{187}Os/^{188}Os_i \approx 1$) during the T-OAE[20] (Fig. 2). The Mochras data show higher $^{187}Os/^{188}Os_i$ values just before the T-OAE CIE (~0.4), which increase to an acme of 0.8 during the T-OAE, and decrease to ~0.3 after the event[23] (Fig. 2). While the absolute $^{187}Os/^{188}Os_i$ values differ between the sites, the magnitude of the excursions at East Tributary and Mochras are similar at 0.4, and are almost half the magnitude observed at Yorkshire (0.7).

The differences observed between the $^{187}Os/^{188}Os_i$ records at East Tributary, Mochras,

and Yorkshire suggest there were regional differences in $^{187}Os/^{188}Os_{sw}$ during the studied interval. These differences likely represent local processes such as differing degrees of hydrographic restriction from the open ocean and the amounts of local runoff and its $^{187}Os/^{188}Os$ composition. However, the similarity in the magnitude of the excursions recorded at East Tributary and Mochras suggest this likely represents the global record of change during the T-OAE. This observation, coupled with the more extreme $^{187}Os/^{188}Os_i$ excursion record at Yorkshire, supports the suggestion that the Yorkshire $^{187}Os/^{188}Os_{sw}$ record was influenced by a local riverine input of radiogenic osmium during the T-OAE[21], and the East Tributary and Mochras records are more representative of global osmium seawater chemistry

With these observations in mind, we advocate, when possible, analyzing osmium isotope records from coeval stratigraphic successions deposited in different sedimentary and ocean basins[18,24,25,26] before attempting to interpret them as a global signal. This methodology is especially important regarding palaeoceanographic studies on intervals older than the Cretaceous since the preserved records are predominantly from continental margin and epicontinental successions, where geochemical signatures have a greater potential to be modified by local processes.

Quantifying the Early Jurassic marine osmium cycle

To gain a more quantitative measure of the changes in the marine osmium cycle during the Toarcian we employed a numerical box model that simulates the osmium inventory of the ocean and its isotopic composition (see Supplemental Information). Specifically, we test whether the osmium isotope excursion associated with the T-OAE (~300 – 500 kyr in duration[31,32]) can be reproduced by a transient increase in the weathering input of radiogenic osmium to the ocean. We also explored other situations that may have potentially driven the observed T-OAE osmium

isotope record, but are likely implausible, such as decreasing the input flux of mantle-derived osmium to zero (see Table 1 for values explored and Supplemental Information for a discussion of these cases). Overall, the numerical model results show that the osmium isotope excursion can be reproduced by a transient three- to six-fold increase in the input of continental-derived osmium to the oceans over 100 to 200 kyr[31,32] (Fig. 4; more details of the modelling results including sensitivity tests can be found in the Supplemental Information).

Changes in the $^{187}Os/^{188}Os_{cont}$ to more radiogenic values through the differential weathering of lithologies such as shales and cratonic rocks[33,34,35] could have played a role in the T-OAE osmium isotope record. We investigated the potential effect this change would have on the osmium budget during the event by running simulations where we elevated $^{187}Os/^{188}Os_{cont}$ from 1.4 to 2 (see Supplemental Information for a discussion of the choice of the maximum $^{187}Os/^{188}Os_{cont}$ value). In these simulations, a nearly three-fold increase of the input of continental-derived osmium to the oceans was still necessary to reproduce the excursion (Fig. 4), regardless of timescale used, and solely increasing $^{187}Os/^{188}Os_{cont}$ to reasonable values cannot reproduce the observed excursion (see Supplemental Information). Given the plausible proposition of the changing composition of the continental weathering flux, we conservatively suggest that T-OAE weathering rates increased by as much as three-fold.

A potential source of radiogenic, continentally derived osmium was the remnants of the Central Pangaean Mountains, a Himalayan-scale mountain belt in eastern North America and northwestern Africa. This mountain belt was positioned at tropical and subtropical latitudes in the Early Jurassic (Fig. 1). The rifting of Pangaea during the Late Triassic and Early Jurassic would have exposed the core of the mountain range leaving this material open to weathering or erosion. General circulation models predict large increases in the air temperature and runoff

184 during the T-OAE in the geographic region that contained these mountains[36]. These regional
185 climatic changes would have facilitated enhanced chemical weathering, and makes this mountain
186 belt a plausible source of the enhanced input of osmium to the oceans advocated here.

187 The weathering of organic-rich rocks and sediments would be another plausible way to
188 raise the isotopic composition of the continental weathering flux, but also results in a net release
189 of CO_2 to the atmosphere[37]. However, enhanced continental runoff would also have increased
190 nutrient delivery and stimulated primary productivity in aquatic environments leading to
191 increased hypoxia, anoxia, and potentially euxinia[5]. Elevated burial of organic matter in these
192 environments would have sequestered much more atmospheric CO_2 than that associated with any
193 black shale weathering, which we suggest represent only a fraction of the continental materials
194 that were predominantly weathered during the event.

195 **Differences in the osmium isotope response between OAE events**

196 A striking feature of the $^{187}Os/^{188}Os$ records during the Mesozoic OAEs is the
197 directionality of their excursions. The T-OAE records show a positive $^{187}Os/^{188}Os$ excursion,
198 whereas the onset of the Cretaceous OAE 1a and OAE 2 both display negative excursions. The
199 difference in the $^{187}Os/^{188}Os$ response to these events most likely lies in the environment where
200 the LIPs were emplaced. The Cretaceous events are associated with subaqueous emplacements
201 of the Ontong Java Plateau (OAE 1a) and the Caribbean and High Arctic LIPs (OAE 2).
202 Emplacement of these LIPs would have supplied large amounts of unradiogenic, mantle-derived
203 osmium directly into the oceans from weathering of basalts on the seafloor, resulting in osmium
204 isotope excursions to nonradiogenic values[25,38,39,40].

205 The T-OAE, on the other hand, is associated with a subaerial emplacement of the Karoo-
206 Ferrar LIP at high latitudes (Fig. 1), where the semi-arid climate would have made the relative

weathering potential of this material low. In contrast to the younger OAEs, the Toarcian $^{187}Os/^{188}Os_i$ records reflect enhancement of the weathering of continental materials facilitated by the injection of greenhouse gases into the atmosphere and subsequent climate changes. Notably, delivery of osmium from the Karoo-Ferrar LIP would have also been delayed, as compared to the Cretaceous LIPs. However, if weathering of the Karoo-Ferrar LIP was a significant source of osmium to the oceans during the T-OAE, then its lower $^{187}Os/^{188}Os$ compositions[41,42,43,44,45] would necessitate an even greater contribution of continental material to generate the observed $^{187}Os/^{188}Os_i$ excursion.

Implications and Conclusions

Based on the osmium isotope records and our modelling results, the transient increase in continental weathering rates during the T-OAE may be one of the largest observed during the Phanerozoic. Chemical weathering rates are also suggested to have significantly increased across the Permian-Triassic boundary[46], Triassic-Jurassic boundary[47,48], and the Paleocene-Eocene Thermal Maximum[49], all of which are associated with intervals of global warming, environmental deterioration, and extinction events[50]. The rapid response of the osmium isotope system during the T-OAE, as well as during other OAEs[38,39,40], indicates that chemical weathering feedbacks may respond to episodes of rapid climatic warming on short timescales ($10^3 – 10^6$ years) and lead to a net drawdown of atmospheric CO_2[5]. Enhanced continental runoff would also have increased nutrient delivery and stimulated primary productivity in nearshore environments, leading to increased marine hypoxia, anoxia, and potentially euxinia[5]. CO_2 would also have been sequestered through the deposition of organic-rich sediments in marine and lacustrine settings[5,6,51].

In the case of the Toarcian OAE, increased weathering likely played a critical role in reversing the enhanced greenhouse state induced by Karoo-Ferrar magmatism. As atmospheric CO_2 was consumed through these mechanisms, global temperatures would have declined[5,20]. As modern atmospheric CO_2 levels continue to increase at rates much higher than any point during the Cenozoic[52], increased weathering, through the chemical and physical weathering feedbacks and stimulation of primary production and subsequent organic matter burial, may eventually act as a negative feedback to global warming, although on timescales much longer than what is necessary to mitigate the immediate environmental and ecological deterioration due to this warming[53].

Methods

$\delta^{13}C$ and total organic carbon analysis

$\delta^{13}C$ and total organic carbon (TOC) were measured from each sample for rhenium, osmium, and trace metals (see below). The samples were prepared and analysed using the same methods from ref 15.

Rhenium and osmium isotopic analysis

In order to isolate primarily the hydrogenous rhenium and osmium from our samples, and minimize the removal of detrital rhenium and osmium, we followed the procedures of ref 54. Between ~0.25 and 1 g of sample powder (dependent upon previously measured rhenium abundances via inductively-coupled plasma mass spectrometry) were digested with a known amount of ^{185}Re and ^{190}Os tracer (spike) solutions in 8 mL of a CrO_3-H_2SO_4 solution; this reaction occurred in sealed Carius tubes, which were heated incrementally to 220 °C for 48

hours. The tubes were allowed to cool before opening. The osmium was immediately isolated and purified from the acid medium by solvent extraction using chloroform. This step was followed by the back reduction of Os from the chloroform into HBr. The Os fraction was further purified by micro-distillation. Rhenium was purified from the remaining CrO_3-H_2SO_4 solution by a NaOH-Acetone solvent extraction[55] and further purified using anion exchange chromatography. The purified Re and Os fractions were then loaded onto Ni and Pt filaments, respectively, and analysed for their isotopic composition using negative thermal-ionization mass spectrometry (NTIMS)[56,57] using a Thermo Scientific TRITON mass spectrometer with static Faraday collection for Re and ion-counting using a secondary electron multiplier in peak-hopping mode for Os. In-house Re and Os solutions were continuously analysed during the course of this study to ensure and monitor long-term mass spectrometry reproducibility. A 125 pg aliquot of the Re std solution and a 50 pg aliquot of DROsS yield $^{185}Re/^{187}Re$ values of 0.5983 ± 0.002 (1 SD, n = 6) and $^{187}Os/^{188}Os$ values of 0.16089 ± 0.0005 (1SD, n = 8), respectively; both are identical to previously reported values[57]. The measured difference in $^{185}Re/^{187}Re$ values for the Re std solution and the accepted $^{185}Re/^{187}Re$ value (0.5974)[58] is used for mass fractionation correction of the Re sample data. All Re and Os data are oxide and blank corrected. Procedural blanks for Re and Os in this study were 12 ± 3 pg/g and 0.07 ± 0.05 pg/g, respectively, with an $^{187}Os/^{188}Os$ value of 0.25 ± 0.15 (n = 4). The $^{187}Re/^{188}Os$ and $^{187}Os/^{188}Os$ uncertainties are determined through full propagation of uncertainties, including those in weighing, mass spectrometer measurements, spike calibrations, blank abundances and reproducibility of standard values.

Trace metal analysis

In order to compare the changes in [Re] and [Os] to sedimentation patterns across the T-OAE, we also analysed the concentrations of aluminum and titanium in each sample, which are used to estimate the contribution of terrigenous input to a sedimentary basin[59,60] (see Fig. 3 and SI dataset). Approximately 0.05g of powder was added to a teflon beaker, followed by the addition of 4 mL of a 50:50 mixture of concentrated HCl and concentrated HNO_3. This solution was placed inside a (CEM MARS 5) microwave assisted digestion system and run until all organic material had broken down at a temperature of 150°C. The samples were then dried down and the silicates were dissolved using 4:1 HNO_3 to HF, dried down, and re-dissolved in 5% HNO_3 solution. A 100μL solution split was spiked with an internal standard to measure elemental abundances using an Agilent 7500cs inductively coupled plasma mass spectrometer in He and H mode. Internal standard was used to correct the samples for machine drift. International standards USGS SCO-1 and SDO-1 were also measured and had a reproducibility of ± 5%.

U-Pb analysis of zircons

CA-TIMS procedures described here are modified from refs 61, 62, 63. After rock samples have undergone standard mineral separation procedures zircons are handpicked in alcohol. The clearest, crack- and inclusion-free grains are selected, photographed, and then annealed in quartz glass crucibles at 900˚C for 60 hours. Annealed grains are transferred into 3.5 mL PFA screwtop beakers, ultrapure HF (up to 50% strength, 500 μL) and HNO_3 (up to 14 N, 50 μL) are added and caps are closed finger tight. The beakers are placed in 125 mL PTFE liners (up to four per liner) and about 2 mL HF and 0.2 mL HNO_3 of the same strength as acid within beakers containing samples are added to the liners. The liners are then slid into stainless steel

299 Parr™ high pressure dissolution devices, which are sealed and brought up to a maximum of
300 200˚C for 8-16 hours (typically 175˚C for 12 hours). Beakers are removed from liners and zircon
301 is separated from leachate. Zircons are rinsed with >18 MΩ.cm water and subboiled acetone.
302 Then 2 mL of subboiled 6N HCl is added and beakers are set on a hotplate at 80˚-130˚C for 30
303 minutes and again rinsed with water and acetone. Masses are estimated from the dimensions
304 (volumes) of grains. Single grains are transferred into clean 300 μL PFA microcapsules
305 (crucibles), and 50 μL 50% HF and 5 μL 14N HNO_3 are added. Each is spiked with a $^{233\text{-}235}$U-
306 ^{205}Pb tracer solution (EARTHTIME ET535), capped, and again placed in a Parr liner (8-15
307 microcapsules per liner). HF and nitric acids in a 10:1 ratio, respectively, are added to the liner,
308 which is then placed in a Parr high pressure device and dissolution is achieved at 220˚C for 40
309 hours. The resulting solutions are dried on a hotplate at 130˚C, 50 μL 6N HCl is added to
310 microcapsules and fluorides are dissolved in high-pressure Parr devices for 12 hours at 180˚C.
311 HCl solutions are transferred into clean 7 mL PFA beakers and dried with 2 μL of 0.5N H_3PO_4.
312 Samples are loaded onto degassed, zone-refined Re filaments in 2 μL of silicic acid emitter[64].

313 Isotopic ratios are measured with a modified single collector 354S (with Sector 54
314 electronics) thermal ionization mass spectrometer equipped with analogue Daly photomultipliers.
315 Analytical blanks are 0.2 pg for U and up to 1.9 pg for Pb. U fractionation was determined
316 directly on individual runs using the EARTHTIME ET535 mixed $^{233\text{-}235}$U-^{205}Pb isotopic tracer
317 and Pb isotopic ratios were corrected for fractionation of 0.25 ± 0.03%/amu, based on replicate
318 analyses of NBS-982 reference material and the values recommended by ref. 65. Data reduction
319 employed the excel-based program of ref. 66. Standard concordia diagrams were constructed and
320 regression intercepts, weighted averages calculated with Isoplot[67]. Unless otherwise noted all
321 errors are quoted at the 2-sigma or 95% level of confidence. Isotopic dates are calculated with

322 the decay constants λ_{238}=1.55125E-10 and λ_{235}=9.8485E-10 (ref. 68) and a $^{238}U/^{235}U$ ratio of
323 137.88. EARTHTIME U-Pb synthetic solutions are analysed on an on-going basis to monitor the
324 accuracy of results.

325 Five single zircon grains from the bentonite at -1.9 meters in the East Tributary section
326 (see Fig. 3) were analysed by the uranium-lead chemical abrasion isotope dilution thermal
327 ionization mass spectrometry technique (U-Pb CA-ID-TIMS). A weighted mean $^{206}Pb/^{238}U$ age
328 of 188.58 ± 0.17 (0.25) [0.32] Ma, (MSWD=0.89) is based on concordant and overlapping
329 results for three of the analysed grains (see SI Dataset 2). Older results for the other two grains
330 suggest that they are xenocrysts and/or contain inherited cores. It is important to note that this
331 bentonite has a previously published multigrain U-Pb ID-TIMS age of 188.3 +1.5/-1 Ma[69].

332 Five single zircon grains from the bentonite at 2.35 meters in the East Tributary section
333 (see Fig. 3) were analysed by the U-Pb CA-ID-TIMS technique. A weighted mean $^{206}Pb/^{238}U$
334 age of 185.49 ± 0.16 (0.25) [0.32] Ma, (MSWD=1.17) is based on concordant and overlapping
335 results for three of the analysed grains (see SI Dataset 3). Older results for the other two grains,
336 one of which is discordant, suggest that they are xenocrysts and/or contain inherited cores.

337

338 **Age model and calculation of $^{187}Os/^{188}Os_i$**

339 The age model (see below) is constructed using a single grain U-Pb CA-ID-TIMS age of
340 188.58 ± 0.17 (0.25) [0.32] Ma from approximately two meters below the lowest interval with
341 carbon isotope data in the East Tributary section[15] and a single grain U-Pb CA-ID-TIMS age of
342 185.49 ± 0.16 (0.25) [0.32] Ma (see above) located at 2.35 meters in the section (see Fig. 3).
343 Linear interpolation was used to calculate ages between the bentonites layers and between the
344 age assigned for the Toarcian CIE. The onset of the CIE is placed at 183.1 Ma, with a total

duration of 300 kyr[31]. Sedimentation rates are also assumed to remain constant after the Toarcian CIE. The initial osmium isotopic composition of the oceans ($^{187}Os/^{188}Os_i$) was calculated using the following equation and the ^{187}Re decay constant from ref. 70:

$$\frac{^{187}Os}{^{188}Os_i} = \frac{^{187}Os}{^{188}Os} - \left(\frac{^{187}Re}{^{188}Os} \times \left(e^{(1.666\times10^{-11}.a^{-1}\times age\times 1000000)} - 1\right)\right) \quad (1)$$

This equation accounts for the ^{187}Os produced after deposition by the decay of ^{187}Re. As stated above, the age component was derived from U-Pb ages from this succession (this study) and previously published dates for the age and estimated duration of the Toarcian CIE[31]. Furthermore, if a longer 500-kyr duration[32] is assigned to the T-OAE CIE, the calculated $^{187}Os/^{188}Os_i$ values do not change significantly and our interpretations do not change (see Supplemental Information).

REFERENCES CITED

1. Walker, J.C.G., Hays, P.B. & Kasting, J.F. A negative feedback mechanism for the long-term stabilization of Earth's surface temperature. *J. Geophys. Res.* **86**, 9776–9782 (1981).
2. Berner, R.A., Lasaga, A.C. & Garrels, R.M. The carbonate-silicate geochemical cycle and its effect on atmospheric carbon dioxide over the past 100 million years. *Am. J. Sci.* **283**, 641–683 (1983).
3. Kump, L.R., Brantley, S.L. & Arthur, M.A. Chemical Weathering, Atmospheric CO_2, and Climate. *Ann. Rev. Earth Plan. Sci.* **28**, 611–667 (2000).
4. Foster, G.L. & Vance, D. Negligible glacial-interglacial variation in continental weathering rates. *Nature* **444**, 918–921 (2006).
5. Jenkyns, H.C. Geochemistry of oceanic anoxic events. *G^3* **11**, Q03004 (2010).
6. Jenkyns, H.C. The Early Toarcian (Jurassic) Anoxic Event: Stratigraphic, Sedimentary, and

Geochemical Evidence. *Am. J. Sci.* **288**, 101–151 (1988).

7. Harries, P.J. & Little, C.T.S. The early Toarcian (Early Jurassic) and the Cenomanian-Turonian (Late Cretaceous) mass extinctions: similarities and contrasts. *Palaeogeo. Palaeoclim. Palaeoecol.* **154**, 39–66 (1999).

8. Pálfy, J. & Smith P.L. Synchrony between Early Jurassic extinction, oceanic anoxic event, and the Karoo-Ferrar flood basalt volcanism. *Geology* **28**, 747–750 (2000).

9. McElwain J.C., Wade-Murphy J. & Hesselbo S.P. Changes in carbon dioxide during an oceanic anoxic event linked to intrusion into Gondwana coals. *Nature* **435**, 479–482 (2005).

10. Beerling, D.J. & Brentnall S.J. Numerical evaluation of mechanisms driving Early Jurassic changes in global carbon cycling. *Geology* **35**, 247–250 (2007).

11. Svensen, H. *et al.* Hydrothermal venting of greenhouse gases triggering Early Jurassic global warming. *Earth Plan. Sci. Lett.* **256**, 554–566 (2007).

12. Hesselbo, S.P. *et al.* Massive dissociation of gas hydrate during a Jurassic oceanic anoxic event. *Nature* **406**, 392–395 (2000).

13. Kemp, D.B., Coe A.L., Cohen A.S. & Schwark L. Astronomical pacing of methane release in the Early Jurassic period. *Nature* **437**, 396–399 (2005).

14. Pieńkowski, G., Hodbod, M. & Ullmann, C.V. Fungal decomposition of terrestrial organic matter accelerated Early Jurassic climate warming. *Scientific Rep.* **6:31030** (2016).

15. Them, T.R. II *et al.* High-resolution carbon isotope records of the Toarcian Oceanic Anoxic Event (Early Jurassic) from North America and implications for the global drivers of the Toarcian carbon cycle. *Earth Plan. Sci. Lett.* **459**, 118–126 (2017).

16. Peucker-Ehrenbrink, B. & Ravizza, G. The marine osmium isotope record. *Terra Nova* **12**, 205–219 (2000).

391 17. Peucker-Ehrenbrink, B. Accretion of extraterrestrial matter during the last 80 million years
392 and its effect on the marine osmium isotope record. *Geochim. Cosmochim. Acta* **60**, 3187–
393 3196 (1996).
394 18. Rooney, A.D. *et al.* Tracking millennial-scale Holocene glacial advance and retreat using
395 osmium isotopes: Insights from the Greenland ice sheet. *Quat. Sci. Rev.* **138**, 49–61 (2016).
396 19. Cohen, A.S., Coe, A.L., Bartlett, J.M. & Hawkesworth, C.J. Precise Re—Os ages of organic-
397 rich mudrocks and the Os isotope composition of Jurassic seawater. *Earth Plan. Sci. Lett.*
398 **167**, 159–173 (1999).
399 20. Cohen, A.S., Coe, A.L., Harding, S.M. & Schwark, L. Osmium isotope evidence for the
400 regulation of atmospheric CO_2 by continental weathering. *Geology* **32**, 157–160 (2004).
401 21. McArthur, J.M., Algeo, T.J., van de Schootbrugge, B., Li, Q. & Howarth, R.J. Basinal
402 restriction, black shales, Re-Os dating, and the Early Toarcian (Jurassic) oceanic anoxic
403 event. *Paleoceanography* **23**, PA4217 (2008).
404 22. Waltham, D. & Gröcke, D.R. Non-uniqueness and interpretation of the seawater $^{87}Sr/^{86}Sr$
405 curve. *Geochim. Cosmochim. Acta* **70**, 384–394 (2006).
406 23. Percival, L.M.E. *et al*. Osmium isotope evidence for two pulses of increased continental
407 weathering linked to Early Jurassic volcanism and climate change. *Geology* **44**, 759–762
408 (2016).
409 24. Paquay, F.S. & Ravizza, G. Hetergeneous seawater $^{187}Os/^{188}Os$ during the Late Pleistocene
410 glaciations. *Earth Plan. Sci. Lett.* **349-350**, 126–138 (2012).
411 25. Du Vivier, A.D.C. *et al.* Marine $^{187}Os/^{188}Os$ isotope stratigraphy reveals the interaction of
412 volcanism and ocean circulation during Oceanic Anoxic Event 2. *Earth Plan. Sci. Lett.* **389**,
413 23–33 (2014).

26. Hall, R.L. Lithostratigraphy and biostratigraphy of the Fernie Formation (Jurassic) in the southern Canadian Rocky Mountains, *in* Stott, D.F. & Glass, D.J., eds., The Mesozoic of Middle North America. *Can. Soc. Petr. Geol. Mem.* **9**, 233–247 (1984).

27. Hall, R.L. New Lower Jurassic ammonite faunas from the Fernie Formation, southern Canadian Rocky Mountains. *Can. J. Earth Sci.* **24**, 1688–1704 (1987).

28. Asgar–Deen, M., Hall, R., Craig, J. & Riediger, C. New biostratigraphic data from the Lower Jurassic Fernie Formation in the subsurface of west-central Alberta and their stratigraphic implications. *Can. J. Earth Sci.* **40**, 45–63 (2003).

29. Porter, S.J., Selby, D., Suzuki, K. & Gröcke, D. Opening of a trans-Pangaean marine corridor during the Early Jurassic: Insights from osmium isotopes across the Sinemurian-Pliensbachian GSSP, Robin Hood's Bay, UK. *Palaeogeo. Palaeoclim. Palaeoecol.* **375**, 50–58 (2013).

30. Cohen, A.S. & Coe, A.L., New geochemical evidence for the onset of volcanism in the Central Atlantic magmatic province and environmental change at the Triassic-Jurassic boundary. *Geology* **30,** 267–270 (2002).

31. Sell, B. *et al.* Evaluating the temporal link between the Karoo LIP and climatic—biologic events of the Toarcian Stage with high-precision U-Pb geochronology. *Earth Plan. Sci. Lett.* **408**, 48–56 (2014).

32. Boulila, S. *et al.* Astronomical calibration of the Toarcian State: Implications for sequence stratigraphy and duration of the early Toarcian OAE. *Earth Plan. Sci. Lett.* **386**, 98–111 (2014).

33. Peucker-Ehrenbrink, B. & Hannigan, R.E. Effect of black shale weathering on the mobility of rhenium and platinum group elements. *Geology* **28**, 475–478 (2000).

34. Jaffe, L.A., Peucker-Ehrenbrink, B. & Petsch S.T. Mobility of rhenium, platinum group elements and organic carbon during black shale weathering. *Earth Plan. Sci. Lett.* **198**, 339–353 (2002).

35. Pierson-Wickmann, A.-C., Reisberg, L. & France-Lanord, C. Behavior of Re and Os during low-temperature alteration: Results from Himalayan soils and altered black shales. *Geochim. Cosmochim. Acta* **66**, 1539–1548 (2002).

36. Dera, G. & Donnadieu, Y. Modeling evidences for global warming, Arctic seawater freshening, and sluggish ocean circulation during the Early Toarcian anoxic event. *Paleoceanography* **27**, PA002283 (2012).

37. Georg, R.B., West, A.J., Vance, D. Newman, K. & Halliday, A.N. Is the marine osmium isotope record a probe for CO_2 release from sedimentary rocks? *Earth Plan. Sci. Lett.* **367**, 28–38 (2013).

38. Tejada, M.L.G. *et al.* Ontong Java Plateau eruption as a trigger for the early Aptian oceanic anoxic event. *Geology* **37**, 855–858 (2009).

39. Bottini, C., Cohen, A.S., Erba, E., Jenkyns, H.C. & Coe, A.L. Osmium-isotope evidence for volcanism, weathering, and ocean mixing during the early Aptian OAE 1a. *Geology* **40**, 583–586 (2012).

40. Turgeon, S.C & Creaser, R.A. Cretaceous oceanic anoxic event 2 triggered by a massive magmatic episode. *Nature* **454**, 323–326 (2008).

41. Ellam, R.M., Carlson, R.W. & Shirey, S.B. Evidence from Re-Os isotopes for plume-lithosphere mixing in Karoo flood basalts genesis *Nature* **359**, 718–721 (1992).

42. Molzahn, M., Reisberg, L. & G. Wörner. Os, Sr, Nd, Pb, O isotope and trace element data from the Ferrar flood basalts, Antarctica: evidence for an enriched subcontinental

lithospheric source. *Earth Plan. Sci. Lett.* **144**, 529–546 (1996).

43. Riley, T.R., Leat, P.T., Storey, B.C., Parkinson, I.J. & Millar, I.L. Ultramafic lamprophyres of the Ferrar large igneous province: evidence for a HIMU mantle component. *Lithos* **66**, 63–76 (2003).

44. Heinonen, J.S., Carlson, R.W. & Luttinen, A.V. Isotopic (Sr, Nd, Pb, and Os) composition of highly magnesian dikes os Vestfjella, western Dronning Maud Land, Antarctica: A key to the origins of the Jurassic large igneous province? *Chem. Geol.* **277**, 227–244 (2010).

45. Heinonen, J.S., Carlson, R.W., Riley, T.R., Luttinen, A.V. & Horan, M.F. Subduction-modified oceanic crust mixed with a depleted mantle reservoir in the sources of the Karoo continental flood basalt province. *Earth Plan. Sci. Lett.* **394**, 229–241 (2014).

46. Sheldon, N.D. Abrupt chemical weathering increase across the Permian-Triassic boundary. *Palaeogeo. Palaeoclim. Palaeoecol.* **231**, 315–321 (2006).

47. Beerling, D.J. & Berner, R.A. Biogeochemical constraints on the Triassic-Jurassic boundary carbon cycle event. *Glob. Biogeo. Cycles* **16**, GB001637 (2002).

48. Kuroda, J., Hori, R.S., Suzuki, K., Gröcke, D.R. & Ohkouchi, N. Marine osmium isotope record across the Triassic-Jurassic boundary from a Pacific pelagic site. *Geology* **38**, 1095–9098 (2010).

49. Ravizza, G., Norris, R.N. & Blusztajn, J. An osmium isotope excursion associated with the late Paleocene thermal maximum: Evidence of intensified chemical weathering. *Paleoceanography* **16**, 155–163 (2001).

50. Hönisch, B., *et al.* The Geological Record of Ocean Acidification. *Science* **335,** 1058–1063 (2012).

51. Xu, W. *et al.* Carbon sequestration in an expanded lake system during the Toarcian oceanic

anoxic event. *Nature Geosci.* **10**, 129–134 (2017).

52. Zeebe, R.E., Ridgwell, A. & Zachos, J.C. Anthropogenic carbon release rate unprecedented during the past 66 million years. *Nature* **9**, 325–329 (2016).

53. Parmesan, C. Ecological and Evolutionary Responses to Recent Climate Change. *Annu. Rev. Ecol. Evol. Syst.* **37**, 637–669 (2006).

54. Selby, D. & Creaser, R.A. Re-Os geochronology of organic rich sediments: an evaluation of organic matter analysis methods. *Chem. Geol.* **200**, 225–240 (2003).

55. Cumming, V.M., Poulton, S.W., Rooney, A.D. & Selby, D. Anoxia in the terrestrial environment during the late Mesoproterozoic. *Geology* **41**, 583–586 (2013).

56. Creaser, R.A., Papanastassiou, D.A. & Wasserburg, G.J. Negative thermal ion mass spectrometry of osmium, rhenium and iridium. *Geochim. Cosmochim. Acta* **55**, 397–401 (1991).

57. Völkening, J., Walczyk, T. & Heumann, K.G. Osmium isotope ratio determination by negative thermal ion mass spectrometry. *Int. J. Mass Spectrom. Ion Process.* **105**, 147–159 (1991).

58. Gramlich, J.W., Murphy, T.J., Garner, E.L. & Shields, W.R. Absolute isotopic abundance ratio and atomic weight of a reference sample of rhenium. *J. Res. Nat. Bur. Stds.* **77A**, 691–698 (1973).

59. Peterson, L.C., Haug, G.H., Hughen, K.A. & Röhl, U. Rapid Changes in the Hydrologic Cycle of the Tropical Atlantic During the Last Glacial. *Science* **290**, 1947–1951 (2000).

60. Latimer, J.C. & Filippelli, G.M. Terrigenous input and paleoproductivity in the Southern Ocean. *Paleoceanography* **16**, 627–643 (2001).

61. Mundil, R., Ludwig, K.R., Metcalfe, I. & Renne, P.R. Age and timing of the Permian Mass

506 Extinctions: U/Pb Dating of Closed-System Zircons. *Science* **305**, 1760–1763 (2004).
507 62. Mattinson, J.M. Zircon U-Pb chemical abrasion ("CA-TIMS") method: Combined annealing
508 and multi-step partial dissolution analysis for improved precision and accuracy of zircon
509 ages. *Chem. Geol.* **220**, 47–66 (2005).
510 63. Scoates, J.S. & Friedman, R.M. Precise age of the platiniferous Merensky Reef, Bushveld
511 Complex, South Africa, by the U-Pb zircon chemical abrasion ID-TIMS technique. *Econ.*
512 *Geol.* **103**, 465–471 (2008).
513 64. Gerstenberger, H. & Haase, G.A. Highly effective emitter substance for mass spectrometric
514 Pb isotopic ratio determinations. *Chem. Geol.* **136**, 309–312 (1997).
515 65. Thirlwall, M.F. Inter-laboratory and other errors in Pb isotope analyses investigated using a
516 207Pb-204Pb double spike. *Chem. Geol.* **163**, 299–322 (2000).
517 66. Schmitz, M.D. & Schoene, B. Derivation of isotope ratios, errors, and error correlations for
518 U-Pb geochronology using 205Pb-235U-(233U)-spiked isotope dilution thermal ionization
519 mass spectrometric data. *Geochem. Geophys. Geosyst.* **8**, Q08006 (2007).
520 67. Ludwig, K.R., Isoplot 3.00, A Geochronological Toolkit for Microsoft Excel. University of
521 California at Berkeley, kludwig@bgc.org.
522 68. Jaffey, A.H., Flynn, K.F., Glendenin, L.E., Bentley, W.C. & Essling, A.M. Precision
523 measurement of half-lives and specific activities of 235U and 238U. *Phys. Rev.* **C4**, 1889–
524 1906 (1971).
525 69. Hall, R., McNicoll, V., Gröcke, D., Craig, J. & Johnston, K. Integrated stratigraphy of the
526 lower and middle Fernie Formation in Alberta and British Columbia, western Canada. *Riv.*
527 *Ital. Paleon. Strat.* **110**, 61–68 (2004).
528 70. Smoliar, M.I., Walker, R.J. & Morgan, J.W. Re-Os ages of Group IIA, IIIA, IVA and IVB

iron meteorites. *Science* **271**, 1099–1102 (1996).

71. Scotese, C.R. Atlas of Earth History. PALEOMAP Project, Arlington, Texas (2001).

Acknowledgements

TRT would like to thank the Virginia Tech College of Science Roundtable grant committee for the Make-a-Difference Scholarship and the ExxonMobil/Geological Society of America, American Association of Petroleum Geologists, and International Association of Sedimentologists graduate student grant programs for funding (IAS grant funded the pilot study). A grant to BCG (EAR-1324752) and JDO (OCE-1624895) from the National Science Foundation also funded this work. DS acknowledges the Total Endowment Fund. Thanks to Dr. Joanna Hesselink, H. Lin, C. Wall, N. Moerhius, and T. Ockerman for laboratory assistance, and to Angela Gerhardt, Emma Tulsky, and Selva Marroquín for their help in collecting samples. Sample collections were authorized by the following permits: Parks Canada, Permit No: YHTR-2014-16156; RTMP, Permit No: 13-058, 14-009, 15-019. Finally, we would like to thank two anonymous reviewers whose comments greatly improved the manuscript.

Author Contributions

TRT, BCG, DS, and DRG designed the study. TRT and BCG collected samples. TRT and DS conducted the Re-Os geochemical analyses. JDO conducted the elemental analyses. RMF conducted the U-Pb CA-ID-TIMS analyses. TRT and BCG conducted the numerical modelling. All authors analysed the data. TRT and BCG wrote the paper with contributions from all the authors. TRT prepared the figures.

Additional Information

Competing financial interests: The authors declare no competing financial interests.

FIGURE CAPTIONS

Figure 1. Global palaeogeography of the Early Toarcian (modified from ref. 71). Star represents this study's location. Arrows point to the UK study locations[20,23], which are geographically close to one another. Hatched outline in southern Pangaea (present-day southern Africa and Antarctica) represents location and known extent of Karoo-Ferrar Large Igneous Province. Dark grey represents landmasses, light blue represents shallow seas, and dark blue represents open oceans. CPM = Central Pangaean Mountains. See ref. 15 for a list of locations that document the T-OAE CIE.

Figure 2: Record of the osmium isotope excursion across the T-OAE CIE from Yorkshire, United Kingdom[20] and the Mochras borehole[23]. The Yorkshire dataset was originally interpreted to represent a 400 – 800% increase in continental weathering rates[20]; however, other interpretations suggests that the radiogenic values during the *exaratum* ammonite subzone were caused by hydrographic restriction[21,22]. The close palaeogeographic proximity between these two sites, coupled with their significantly different $^{187}Os/^{188}Os_i$ values suggests a regional influence on $^{187}Os/^{188}Os_{sw}$ values in the European epicontinental seaway during the T-OAE.

Figure 3: Chemostratigraphy of the Lower Jurassic Fernie Formation from East Tributary of Bighorn Creek Alberta. $\delta^{13}C_{org}$ = organic carbon isotopic compositions from ref. 15. $^{187}Os/^{188}Os_i$ = initial osmium isotopic composition of organic-rich sediments. Lithostratigraphic members of the Fernie Formation, Stages of the Jurassic, and ammonite zonations for both northwestern

575 Europe and western North American shown to the left of the stratigraphic column (refer to ref.
576 15 for the details of their placements). Vertical gray line in $^{187}Os/^{188}Os_i$ record is the end-member
577 $^{187}Os/^{188}Os_m$ value of ~0.12. We report new single zircon U-Pb CA-ID-TIMS ages of 188.58 ±
578 0.17 (0.25) [0.32] Ma in the bentonite at -1.9 meters and 185.49 ± 0.16 (0.25) [0.32] Ma in the
579 bentonite at 2.35 meters, located in the *margaritatus* Zone of NW Europe or the *kunae* Zone of
580 western NA (see Methods and SI Data 2).
581
582 Figure 4: Examples of the modelled osmium isotopic composition of the ocean over the T-OAE.
583 **A)** For this model run, the osmium isotopic composition of the continental input was increased to
584 2.0 and the flux of osmium from continents was increased two-fold (475.3 mol/yr) during the
585 Toarcian OAE. This resulted in the seawater osmium isotope values to increase to 0.44, which
586 does not reproduce the observed osmium isotope excursion observed at East Tributary. **B)** Model
587 run where the osmium isotopic composition and flux of the continental input of osmium was
588 increased to 2.0 by ~3.4x respectively. This model run reproduced the osmium isotope
589 excursion. **C)** The osmium isotope composition of the continental input of osmium was kept at
590 1.4 during the Toarcian OAE, but the flux of osmium from continents was increased by ~6.3x to
591 reproduce the osmium isotope excursion.
592
593 **Table**
594 Table 1. Range of parameters explored modelling the osmium isotope excursion associated with
595 the Toarcian Oceanic Anoxic Event in the East Tributary and Yorkshire sections.

Model parameter	Pre- and post-T-OAE steady state	OAE state
M_{SW}[a]	10^5 to 10^9	10^5 to 10^9
F_{cont}[b]	238 to 524	238 to 5,500
N_{cont}	1.4 to 2.0	1.4 to 5.0
F_m[b]	1,925 to 2,212	0 to 2,212
N_m	0.12	0.12
Duration[c]		300 to 500

[a] Reservoir unit is mol Os
[b] Flux units are mol/yr Os
[c] Duration unit is kiloyear (kyr)

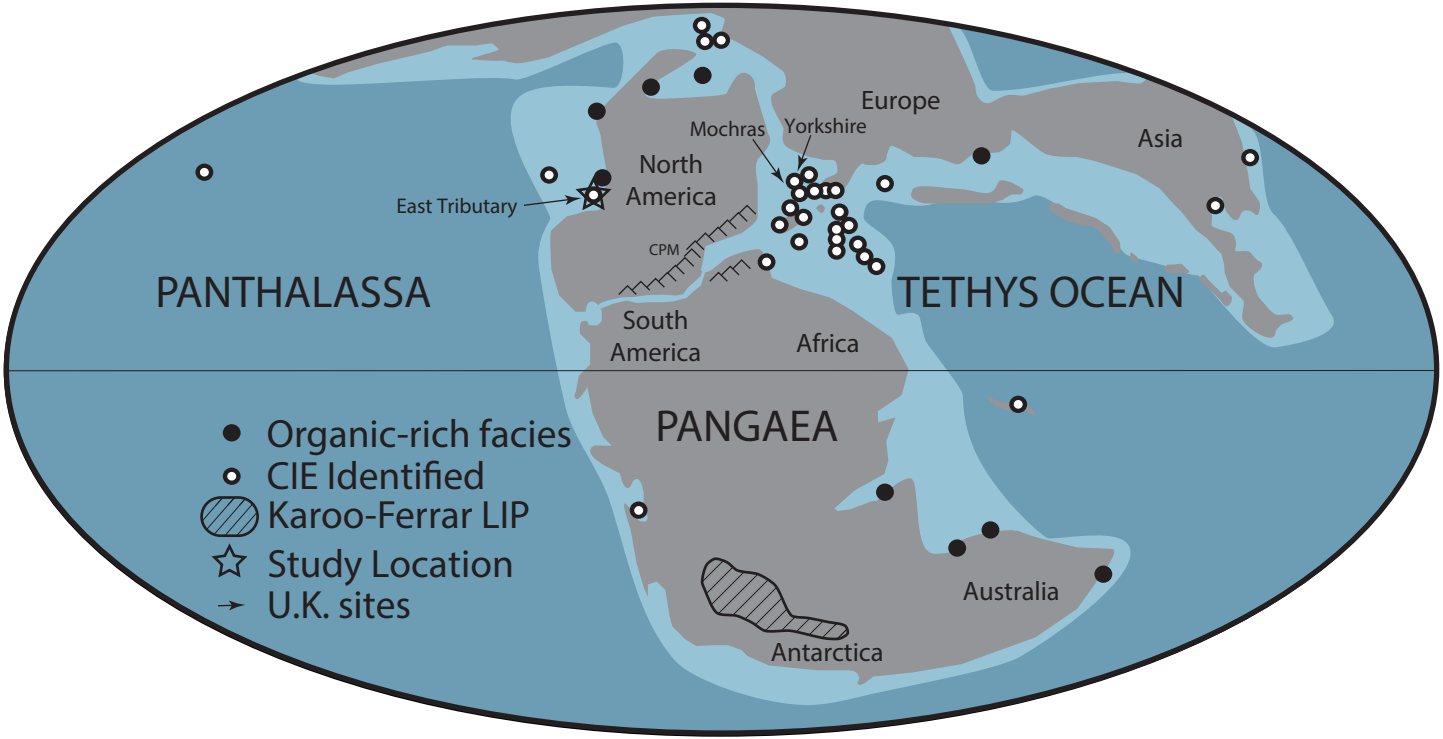
Europe
Mochras
Yorkshire
Asia
North
America
East Tributary
CPM
PANTHALASSA
TETHYS OCEAN
South
America
Africa
PANGAEA
Organic-rich facies
CIE Identified
Karoo-Ferrar LIP
Study Location
U.K. sites
Australia
Antarctica

Stage
W.North America
N.W.Europe
Mediterranean
Toarcian
kanense
planulata
serpentinum
bifrons
tenuicostatum
levisoni
polymorphum
Yorkshire
-33
-31
-29
-27
-25
δ13Corg (‰ VPDB)
0.2
0.4
0.6
0.8
1.0
187Os/188Osi

Stage
W.North America
N.W.Europe
Mediterranean
Pliensbachian
carlottense
spinatum
emaciatum
Toarcian
kanense
plan.
bif.
tenuicostatum
serpentinum
polymorphum
levisoni
Mochras
-32
-30
-28
-26
-24
δ13Corg (‰ VPDB)
0.2
0.4
0.6
0.8
1.0
187Os/188Osi

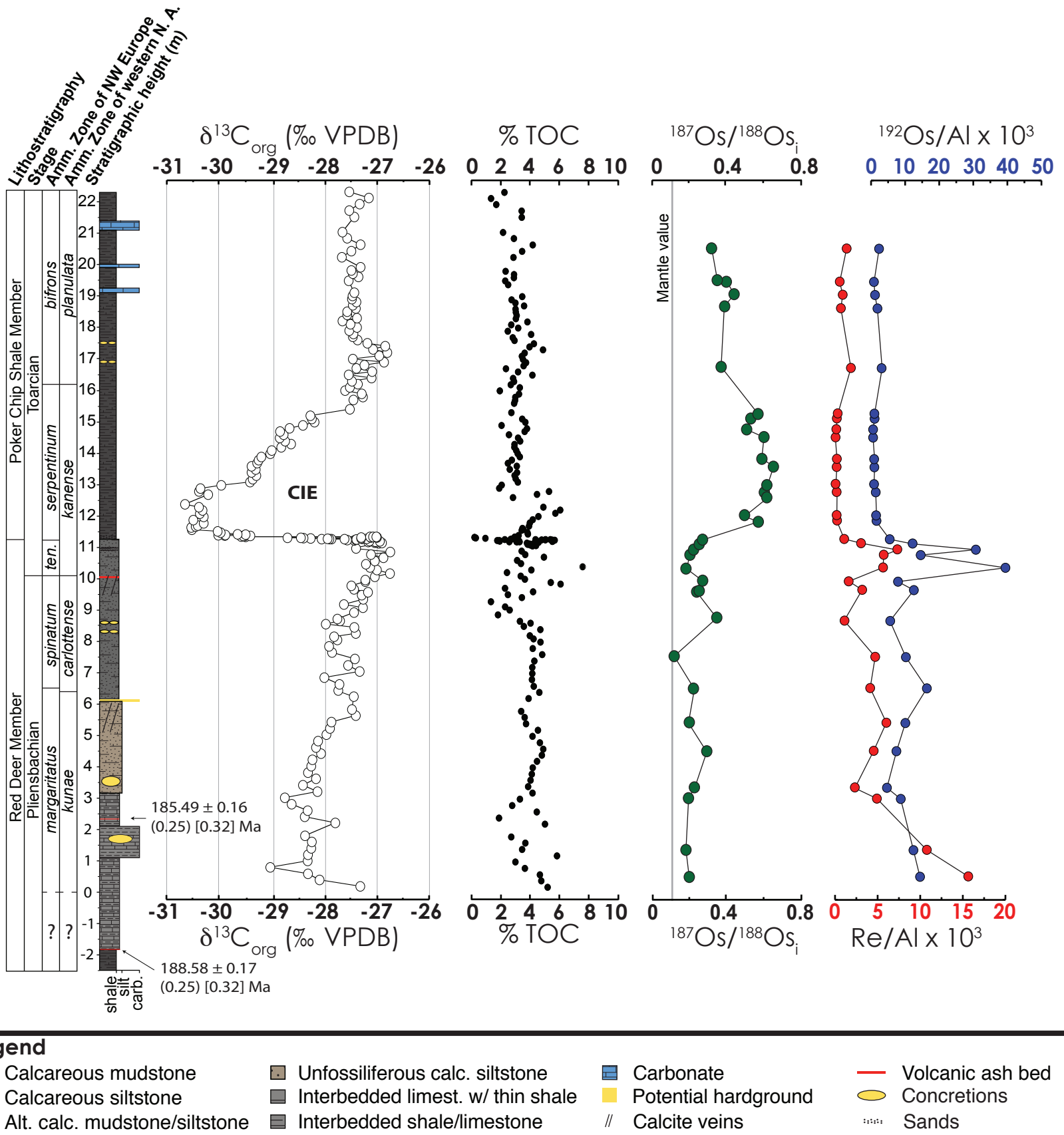

Legend

- Calcareous mudstone
- Calcareous siltstone
- Alt. calc. mudstone/siltstone
- Unfossiliferous calc. siltstone
- Interbedded limest. w/ thin shale
- Interbedded shale/limestone
- Carbonate
- Potential hardground
- // Calcite veins
- Volcanic ash bed
- Concretions
- Sands

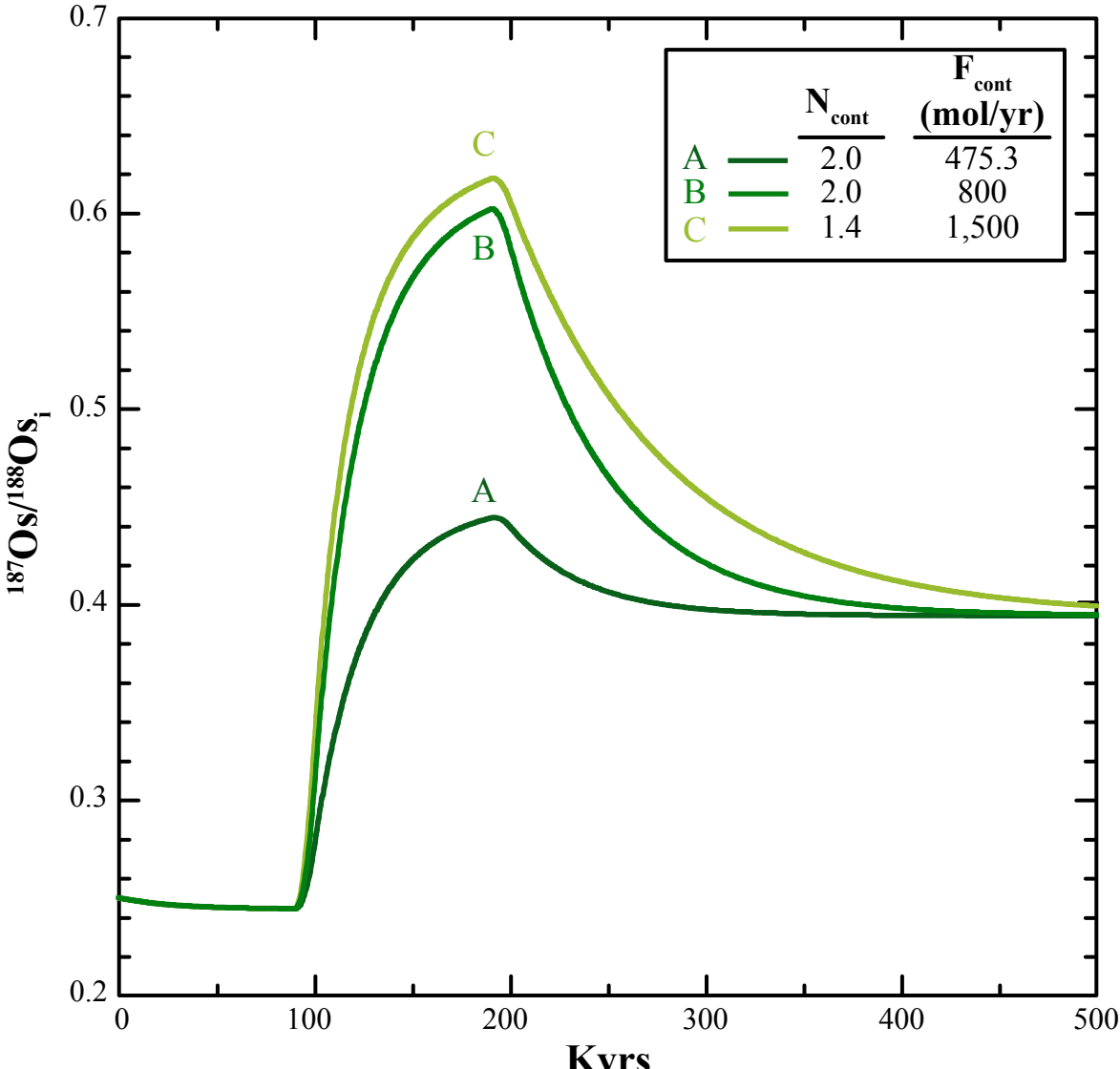
0.7
0.6
0.5
0.4
0.3
0.2
$^{187}Os/^{188}Os_i$
0
100
200
300
400
500
Kyrs
A
B
C
N_{cont}
F_{cont} (mol/yr)
A 2.0 475.3
B 2.0 800
C 1.4 1,500

Supplemental Information for:

Evidence for rapid weathering response to climatic warming during the Toarcian Oceanic Anoxic Event

Theodore R. Them II[1,2*], Benjamin C. Gill[1], David Selby[3], Darren R. Gröcke[3], Richard M. Friedman[4], and Jeremy D. Owens[2]

SUPPLEMENTAL INFORMATION

Estimating continental and oceanic contributions of osmium to the global oceans

In order to better determine what processes could result in the observed osmium isotope excursion, we built a forward box model of the osmium cycle (SI Fig. 1). The change in the osmium isotope composition of the ocean was calculated using the following equation:

$$\frac{dN_{SW}}{dt} = \frac{F_{cont}\left(N_{cont} - N_{SW}\right) + F_{M}\left(N_{M} - N_{SW}\right)}{M_{SW}} \quad (1)$$

where dN_{SW}/dt represents the change in the osmium isotopic composition of seawater with time, N_{SW} represents the osmium isotopic composition of seawater; F_{cont} represents the flux of radiogenic, continental osmium from rivers, and N_{cont} represents its isotopic composition; F_m represents the flux of unradiogenic, mantle osmium from the alteration of juvenile oceanic crust and hydrothermal fluids, and N_m represents the osmium isotopic composition of this input; and M_{SW} represents the global inventory of oceanic osmium.

We calibrated our model to the modern osmium cycle and utilized the flux estimate of osmium to the oceans from the riverine input of 1800 moles Os yr^{-1} with an isotopic composition of 1.4 and an ocean inventory of $7x10^7$ moles Os (Peucker-Ehrenbrink & Ravizza, 2000 and references therein). In order for the ocean reservoir to maintain isotopic steady state (dN_{SW}/dt =

0) at the modern marine isotope composition of 1.06, a flux of osmium from the mantle of 650 moles Os yr^{-1} with an isotope composition of 0.12 is required. To maintain mass balance, the flux of osmium sequestered in sediments was set to 2450 moles Os yr^{-1}.

Estimating continental and oceanic contributions of osmium to the Jurassic global oceans

In the following calculations, we initially set the total Jurassic input of osmium to the oceans at the modern estimate of 2450 moles Os yr^{-1} (previously calculated using values from Peucker-Ehrenbrink and Ravizza, 2000 and the steady state model above). In order to reach a pre-Toarcian OAE steady-state $^{187}Os/^{188}Os_{sw}$ value of ~0.25, the continental and mantle inputs of osmium to the ocean were set at 238 moles Os yr^{-1} ($^{187}Os/^{188}Os_{cont}$ = 1.4) and 2,210 moles Os yr^{-1} ($^{187}Os/^{188}Os_{m}$ = 0.12), respectively. If the global input of osmium to the Jurassic oceans was much higher or lower than today, then these fluxes can be scaled accordingly in order to maintain isotopic steady state. We also note, the different pre-event $^{187}Os/^{188}Os_{sw}$ observed at Mochras could be achieved with slightly higher F_{cont} and/or $^{187}Os/^{188}Os_{cont}$. Using the above isotopic compositions, the unradiogenic, F_m was roughly 90% of the flux of osmium to the oceans and the radiogenic, F_{cont} was only approximately 10% before the Toarcian OAE. As stated above, we have not included the flux of osmium from cosmic dust or aeolian dust since these are thought to be minor inputs to the ocean, and the cosmic flux is generally assumed constant (Peucker-Ehrenbrink, 1996).

Based on our knowledge of the marine osmium cycle, several scenarios could have potentially produced the Toarcian osmium isotope record recorded at the East Tributary section based on the directionality of the excursion. These include transiently 1) increasing F_{cont}, 2) increasing N_{cont}, 3) increasing both F_{cont} and N_{cont}, 4) decreasing F_m. We therefore conducted a series of simulations and sensitivity tests using the model in order to identify scenarios that

produced acceptable results (i.e. reproduced the magnitude and duration of the observed osmium isotope excursion). Across our simulations, durations of 100 to 300 kyrs for the transient change in the osmium cycle produced positive excursions with durations of 300 to 500 kyrs (SI Fig. 2) and are consistent with estimates for the duration of the overall osmium isotope excursion (Sell et al., 2014; Boulila et al., 2014).

Solely increasing F_{cont} or increasing both F_{cont} and N_{cont} produced solutions that reproduced the observed Os isotope record. For an example of scenario 1, increasing the F_{cont} for 100 kyr from 238 mol Os yr^{-1} to 1,500 mol Os yr^{-1} reproduced the magnitude and timing of the observed isotope excursion. Increasing N_{cont} in conjunction with F_{cont} decreases the needed increase in F_{cont} (see discussion below on solely changing the isotopic composition of the riverine flux). For an example of scenario 3, changing N_{cont} from 1.4 to 2.0, and increasing the F_{cont} from 238 mol Os yr^{-1} to 800 mol Os yr^{-1} for 100 kyr, resulted in an acceptable solution. Broadly across our simulations, increases in F_{cont} of 238 to 1,500 moles per year depending model conditions (e.g., the value(s) of N_{cont}) could reproduce the Toarcian osmium isotope excursion.

Other scenarios also produced acceptable numerical solutions; however, these represent geologically unlikely scenarios. For example, it is possible to reproduce the isotope excursion by changing only the isotopic composition of osmium entering the oceans from continents. However, this requires that, at a minimum, $^{187}Os/^{188}Os_{cont}$ values transiently increase to 5. The highest recorded modern riverine $^{187}Os/^{188}Os$ values were found within Mackenzie River basin at 3 – 4.5, and these compositions were isolated to only a few tributaries within the watershed. These tributaries do, however, cause the Mackenzie River to be slightly more radiogenic ($^{187}Os/^{188}Os$ = 1.5-1.7) than the world river average $^{187}Os/^{188}Os$ of 1.4 (Huh et al., 2004).

Therefore, we conclude that it is unlikely that global $^{187}Os/^{188}Os_{cont}$ values increased to values much greater than 2 during the T-OAE (Cohen et al., 2004).

Simulations where F_m was transiently reduced did not produce acceptable solutions. For example, eliminating the mantle flux for 100 kyrs yields an excursion with a maximum value of only 0.55. Further, this is also an unrealistic scenario as there is no reasonable way to explain why the weathering of unradiogenic mafic materials (CAMP basalts, juvenile oceanic crust, etc.) would cease during the event.

It is also important to note that decreasing the M_{SW} inventory does not significantly alter the needed increase in F_{cont} or N_{cont} necessary to generate the osmium isotope excursion (SI Fig. 3 displays example sensitivity tests of varying M_{SW}). This is due to the relatively short residence time of Os (Toarcian residence times explored here: 10 to 90 kyrs) in the ocean as compared to the duration of the osmium isotope excursion. This is important because with the expansion of marine anoxia during the event, it is plausible that the Os reservoir was significantly reduced. Reducing M_{SW} does, however, affect how quickly N_{SW} reaches its peak value (SI Fig. 3). However, simulations with M_{SW} less than a third of the modern marine inventory produced osmium isotope excursions with rising limbs that were shorter than the minimum estimated durations (~100 kyrs) inferred from the Toarcian osmium isotope records (Cohen et al., 2004; Percival et al., 2016; this study). This, therefore, places a limit on the potential decrease in M_{SW} due to the expansion of anoxia during the T-OAE. Increasing M_{SW} over an order of magnitude greater than modern reservoir produced rising limbs that were too long (greater than 250 kyrs) or the excursion did not reach the observed peak in $^{187}Os/^{188}Os$. These sensitivity tests suggest that M_{SW} was within an order of magnitude of the size of modern marine reservoir.

We also simulated the effects of changing the duration of the changes in the osmium cycle would have on the duration of the osmium isotope excursion (SI Fig. 2). We tested three scenarios, a) transiently and instantaneously increasing F_{cont} and N_{cont} for 100 kyrs followed by a return to a new steady state, b) increasing F_{cont} and N_{cont} in 20 kyrs steps over 100 kyr, letting F_{cont} and N_{cont} remain constant for 100 kyr, and then decreasing F_{cont} and N_{cont} in 20 kyr steps over 100 kyrs (300 kyrs of total perturbation), and c) increasing F_{cont} and N_{cont} in 40 kyr steps over 200 kyr, letting F_{cont} and N_{cont} remain constant for 100 kyr, and then decreasing F_{cont} and N_{cont} in 40 kyr steps over 200 kyr (500 kyrs of total perturbation). The 100-kyr and 300-kyr perturbations produced excursions that satisfy the U-Pb estimation from South America (Sell et al., 2014), and the 500-kyr perturbation satisfies the astronomical calibration from Europe (Boulila et al., 2014).

We also reproduced the osmium isotope excursion from Yorkshire to test whether plausible scenarios could produce that osmium isotope record (Fig. 2 of main text) (Cohen et al., 2004). For example, increasing the flux of osmium from continents from 238 to 5,500 mol Os yr^{-1} for 100 kyr (using pre-OAE steady-state conditions calculated from the Alberta osmium dataset) can reproduce the magnitude and timing of the observed Yorkshire osmium isotope excursion (see SI Fig. 4). This constitutes an increase of ~2,200% above the pre-T-OAE riverine flux values. Also, changing the osmium isotopic composition of the continental end-member from 1.4 to 2.0, and increased the flux of continental-derived osmium from 238 to 2,100 mol Os yr^{-1} (an increase in riverine osmium delivery of ~800%) for 100 kyr resulted in an acceptable solution (see SI Fig. 4). However, both of these values require an extremely large (and likely unreasonable) increase in the riverine flux to the ocean if the Yorkshire dataset is indicative of a global signal. Therefore, it is unlikely that this record reflects the $^{187}Os/^{188}Os$ evolution of the

115 global ocean and was probably modified by local/regional riverine inputs during the T-OAE
116 (McArthur et al. 2008). As such, the long-term Yorkshire $^{187}Os/^{188}Os$ record is identical to that of
117 the Mochras borehole (Percival et al., 2016) and northeastern Panthalassa (this study).
118
119 **SI FIGURE CAPTIONS**
120
121 SI Figure 1. The exogenic osmium cycle (modified from Peucker-Ehrenbrink and Ravizza,
122 2000). The major inputs of osmium to oceans are from the weathering of materials from the
123 continents ($^{187}Os/^{188}Os_{cont} \approx 1.4$) and the alteration of juvenile oceanic crust ($^{187}Os/^{188}Os_{m} \approx$
124 0.12). Sequestration of the seawater inventory of osmium occurs during precipitation of iron-
125 manganese crusts on the ocean bottom and through biological uptake associated with primary
126 productivity and burial in sediments.
127
128 SI Figure 2. Examples of the modelled osmium isotopic composition of the ocean over the T-
129 OAE when changing the duration of the T-OAE. **A)** For this model run, F_{cont} and N_{cont} were
130 transiently and instantaneously increased for 100 kyr followed by a return to a new steady-state
131 **B)** Model run where F_{cont} and N_{cont} were increased in 20-kyr steps over 100 kyr, F_{cont} and N_{cont}
132 remained constant for 100 kyr, and then F_{cont} and N_{cont} were decreased in 20-kyr steps over 100
133 kyr, and **C)** Model run where F_{cont} and N_{cont} were increased in 40 kyr steps over 200 kyr, F_{cont}
134 and N_{cont} remained constant for 100 kyr, and then F_{cont} and N_{cont} were decreased in 40 kyr-steps
135 over 200 kyr. Model A required an increase in weathering rates of 230%, whereas model runs B
136 and C required an increase in weathering rates of 215%. Therefore, changing the duration of the

T-OAE does not significantly change our interpretations of increased weathering rates; it does, however, result in different overall amounts of osmium added into the ocean during the event.

SI Figure 3. Examples of the modeled osmium isotopic composition of the ocean over the T-OAE when only changing M_{ocean}. **A)** For this model run, M_{ocean} was set to $7x10^5$ moles **B)** Model run where M_{ocean} was set to $7x10^6$ moles **C)** Model run where M_{ocean} was set to $7x10^7$ moles (modern M_{ocean} value) **D)** Model run where M_{ocean} was set to $7x10^8$ moles **E)** Model run where M_{ocean} was set to $7x10^9$ moles. F_{cont} and N_{cont} remained constant for each simulation, and a step function was used to increase and decrease both parameters for 100 kyr.

SI Figure 4. Examples of the modeled osmium isotopic composition of the ocean over the T-OAE in order to replicate the Yorkshire $^{187}Os/^{188}Os_i$ record. **A)** For this model run, the N_{cont} was constant ($^{187}Os/^{188}Os_{cont}$ = 1.4) and the F_{cont} was increased to 5,500 mol/yr during the T-OAE. This resulted in the seawater osmium isotope values to increase to 1. **B)** Model run where N_{cont} was increased to 2.0 during the T-OAE, and F_{cont} was increased to 2,100 mol/yr. Both of these scenarios suggest an unrealistic increase in the amount of osmium delivered from the continents during the T-OAE.

REFERENCE CITED FOR SUPPLEMENTARY INFORMATION

Boulila, S. *et al.* Astronomical calibration of the Toarcian State: Implications for sequence stratigraphy and duration of the early Toarcian OAE. *Earth Plan. Sci. Lett.* **386**, 98–111 (2014).

159 Cohen, A.S. The rhenium-osmium isotope system: applications to palaeoenvironmental
160 problems. *J. Geol. Soc. Lon.* **161**, 729–734 (2004).
161 Cohen, A.S., Coe, A.L., Harding, S.M. & Schwark, L. Osmium isotope evidence for the
162 regulation of atmospheric CO_2 by continental weathering. *Geology* **32**, 157– 160 (2004).
163 Esser, B.K. & Turekian, K.K. The osmium isotopic composition of the continental crust.
164 *Geochim. Cosmochim. Acta* **57**, 3093–3104 (1993).
165 Huh, Y., Birck, J.-L. & Allègre, C.J. Osmium isotope geochemistry in the Mackenzie River
166 basin. *Earth Plan. Sci. Lett.* **222**, 115–29 (2004).
167 McArthur, J.M., Algeo, T.J., van de Schootbrugge, B., Li, Q. & Howarth, R.J. Basinal
168 restriction, black shales, Re-Os dating, and the Early Toarcian (Jurassic) oceanic anoxic
169 event. *Paleoceanography* **23**, PA4217 (2008).
170 Percival, L.M.E., Cohen, A.S., Davies, M.K., Dickson, A.J., Hesselbo, S.P., Jenkyns, H.C.,
171 Leng, M.J., Mather, T.A., Storm, M.S. & Xu. W. Osmium isotope evidence for two pulses
172 of increased continental weathering linked to Early Jurassic volcanism and climate change.
173 *Geology* **44**, 759– 762 (2016).
174 Peucker-Ehrenbrink, B. Accretion of extraterrestrial matter during the last 80 million years and
175 its effect on the marine osmium isotope record. *Geochim. Cosmochim. Acta* **60**, 3187–3196
176 (1996).
177 Peucker-Ehrenbrink, B. Comment on "Residence time of osmium in the oceans" by Rachel
178 Oxburgh. *G^3* **3**, 1–4 (2002).
179 Peucker-Ehrenbrink, B. & Ravizza, G. The marine osmium isotope record. *Terra Nova* **12**, 205–
180 219 (2000).

Sell, B., Ovtcharova, M., Guex, J., Bartolini, A., Jourdan, F., Spangenberg, J.E., Vicente, J.-C. & Schaltegger, U. Evaluating the temporal link between the Karoo LIP and climatic—biologic events of the Toarcian Stage with high-precision U-Pb geochronology. *Earth Plan. Sci. Lett.* **408**, 48–56 (2014).

Them, T.R. II, Gill, B.C., Caruthers, A.H., Gröcke, D.R., Tulsky, E.T., Martindale, R.C., Poulton, T.P. & Smith, P.L. High-resolution carbon isotope records of the Toarcian Oceanic Anoxic Event (Early Jurassic) from North America and implications for the global drivers of the Toarcian carbon cycle. *Earth Plan. Sci. Lett.* doi: 10.1016/j.epsl.2016.11.021.

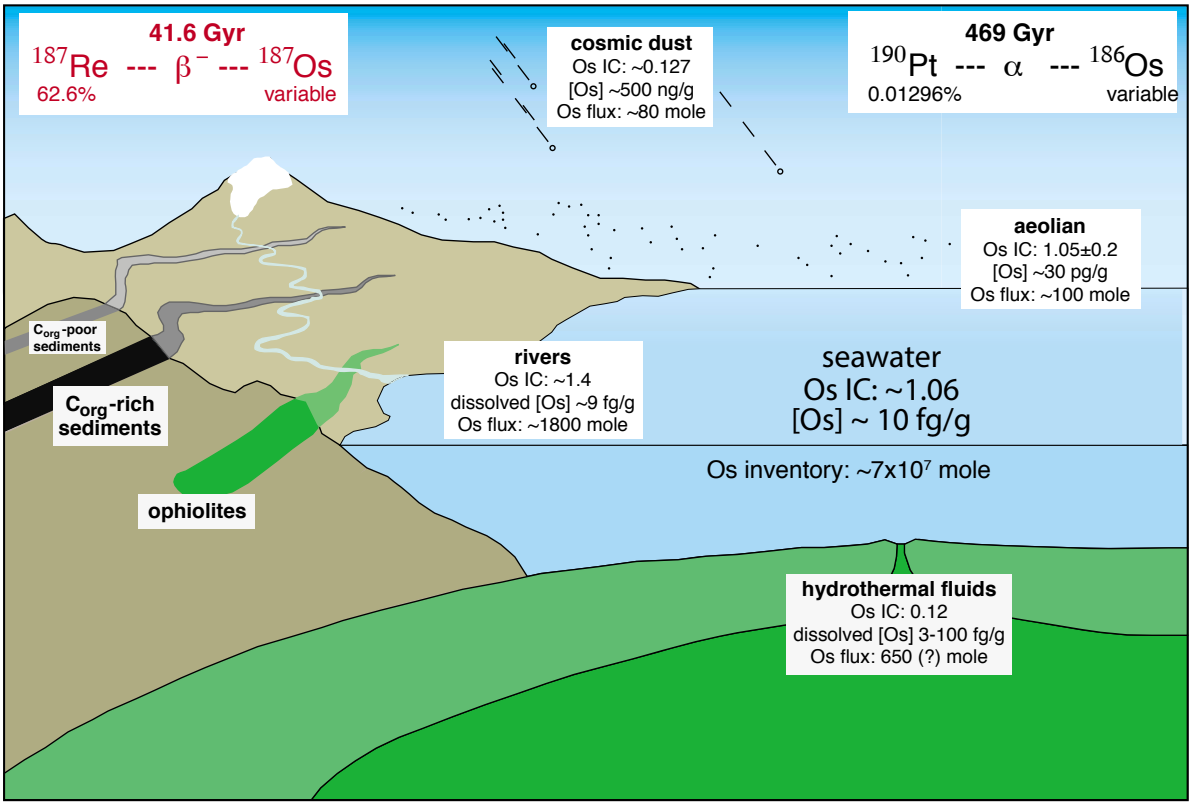

SI Figure 1.

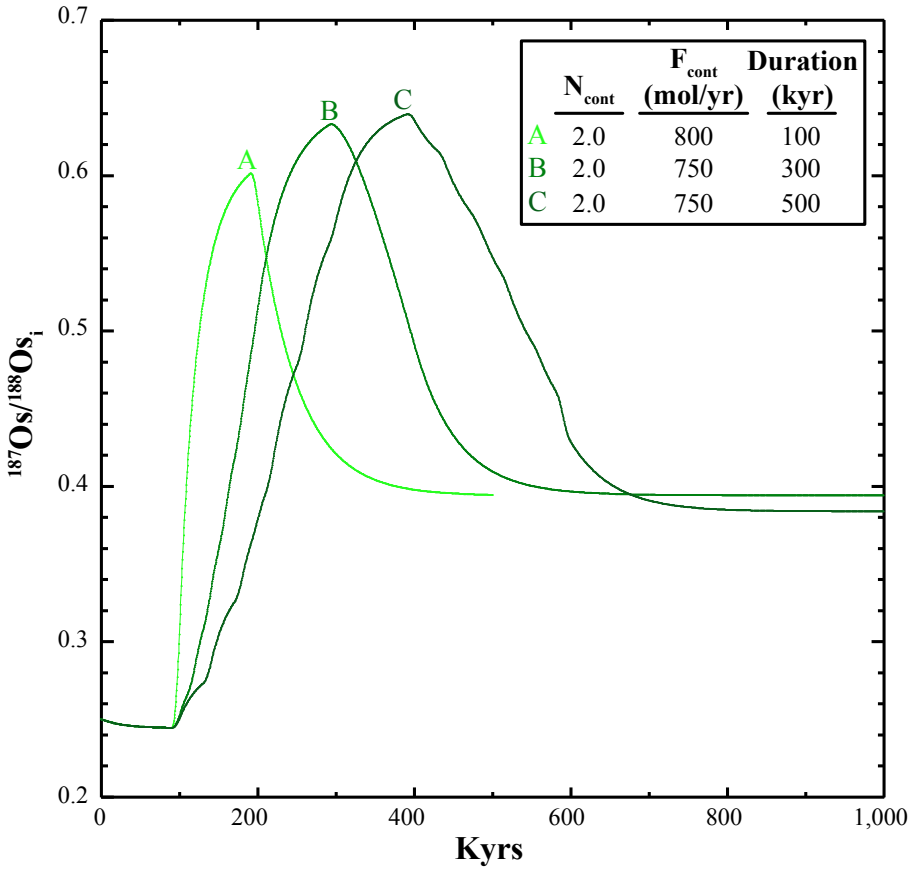

193

194 SI Figure 2.

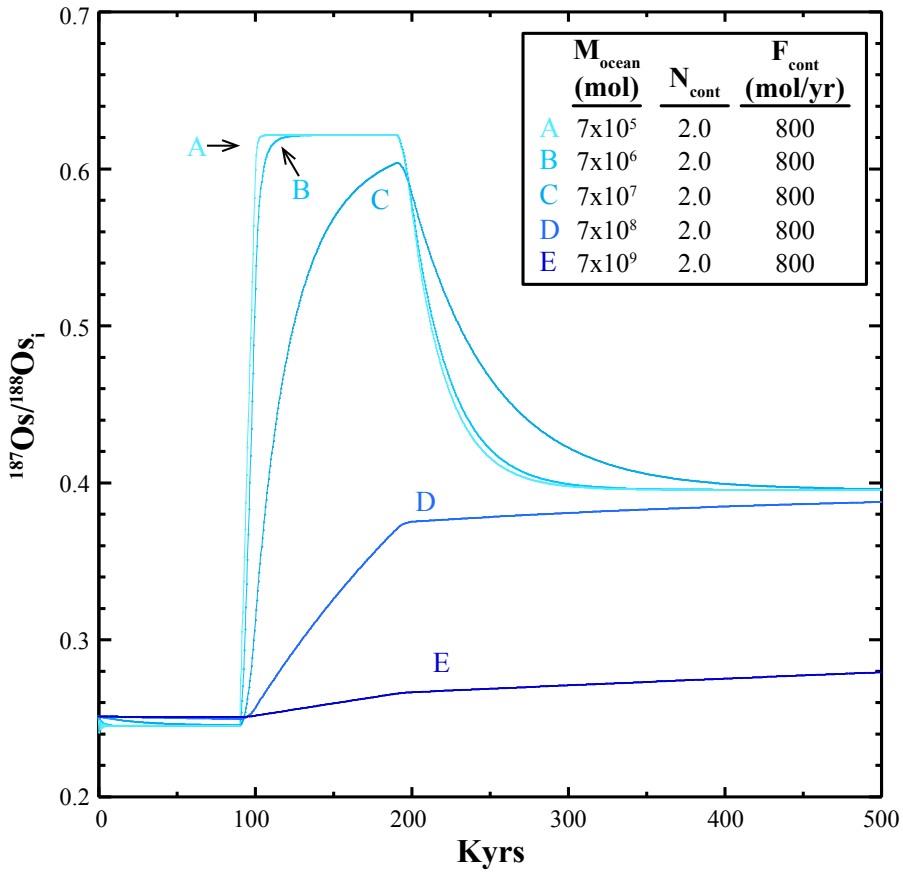

195

196 SI Figure 3.

197

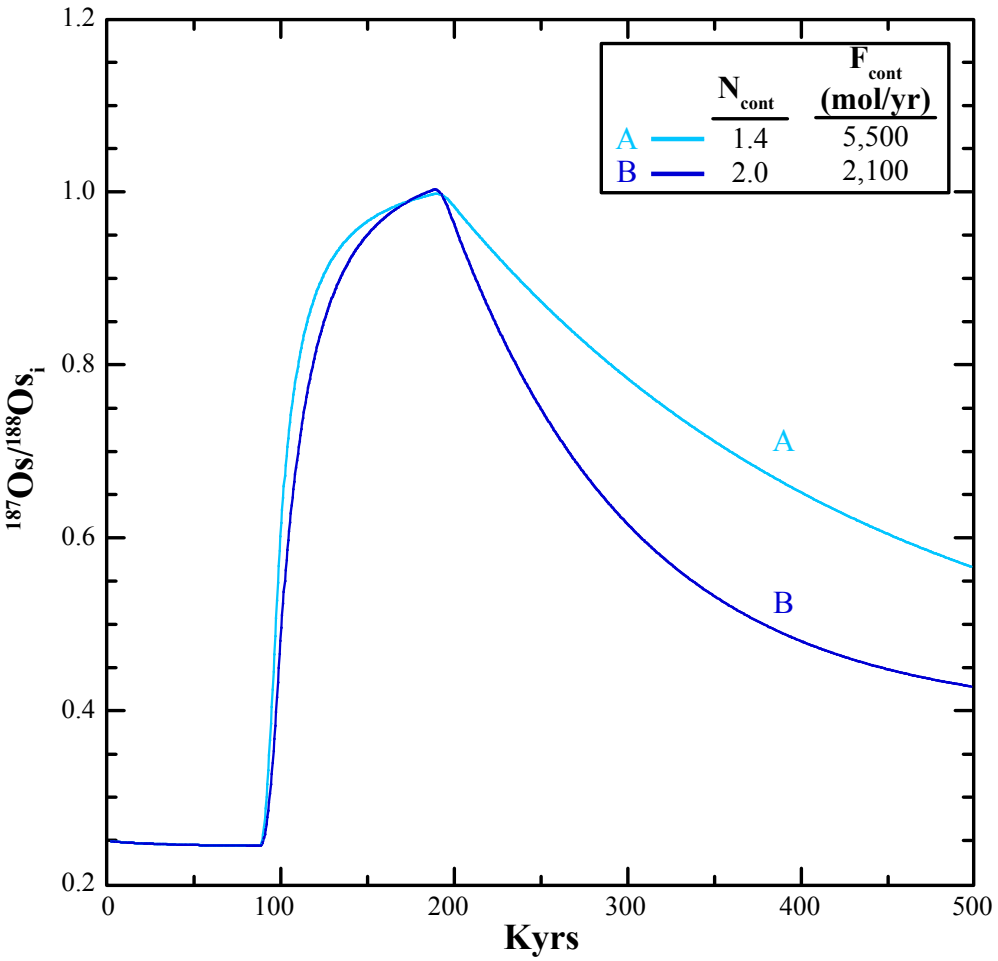

198

199 SI Figure 4.

Batch/Sample	Stratigraphic height (m)	Age (Ma)	Re (ppb)	±	Os (ppt)	±
RO835-2_ET30	0.5	186.839412	258.9	0.6	1088.3	7.2
RO835-1_ET29	1.35	186.219412	145.0	0.4	691.9	4.4
RO718-6_ET27	2.99	185.318443	38.5	0.1	241.6	1.5
RO718-7_ET28	3.33	185.22730	61.4	0.2	421.4	2.5
RO718-5_ET26	4.5	184.913677	72.5	0.2	433.8	2.7
RO718-4_ET25	5.4	184.67242	76.1	0.2	457.5	2.7
RO718-1_ET31	6.5	184.377562	62.6	0.2	730.2	3.3
RO718-3_ET24	7.5	184.109504	98.8	0.2	710.4	3.8
RO718-2_ET23	8.65	183.801238	32.3	0.1	467.3	2.3
RO597-10_ET54	9.6	183.546584	39.6	0.1	495.0	2.5
RO626-8_ET6	9.63	183.538542	33.9	0.1	394.2	2.4
RO622-3_ET-5	9.9	183.466166	31.1	0.1	440.2	2.3
RO626-7_ET4	10.35	183.345541	54.6	0.2	1037.4	4.0
RO626-6_ET2	10.75	183.238318	58.6	0.1	430.3	2.5
RO622-2_ET-3	10.92	183.192748	77.7	0.3	952.5	3.5
RO622-1_ET-1	11.12	183.139136	79.7	0.3	936.0	3.3
RO622-4_ET-7	11.26	183.101608	55.8	0.2	814.3	3.5
RO629-1_ET-8	11.84	183.065099	9.8	0.0	187.1	1.3
RO622-5_ET-9	12.02	183.054155	8.7	0.0	187.0	1.2
RO597-11_ET81	12.6	183.018889	17.4	0.1	239.5	1.9
RO629-2_ET-10	12.75	183.009769	12.9	0.0	266.3	1.5
RO622-6_ET-11	13	182.994568	4.8	0.0	160.4	1.0
RO629-3_ET-12	13.55	182.961127	9.4	0.0	140.9	1.1
RO626-1_ET13	13.8	182.945926	9.0	0.0	119.6	1.0
RO629-4_ET-14	14.5	182.903364	3.9	0.0	103.8	0.7
RO626-2_ET15	14.75	182.888164	9.6	0.0	121.5	1.0
RO629-5_ET-16	15.1	182.866883	8.0	0.0	115.1	0.9
RO626-3_ET17	15.25	182.857762	11.6	0.0	116.0	0.9
RO629-8_ET-22	16.7	182.769599	82.9	0.3	502.9	2.9
RO626-5_ET21	18.6	182.654074	33.8	0.2	340.2	2.4
RO629-6_ET-18	19.03	182.627929	72.4	0.3	376.3	2.6
RO626-4_ET19	19.45	182.602392	54.6	0.2	314.9	2.3
RO597-12_ET145	19.5	182.599351	48.7	0.2	368.9	2.4
RO629-7_ET-20	20.51	182.537941	85.6	0.3	530.3	3.0

192Os (ppt)	±	187Re/188Os	±	187Os/188Os	±	rho	d13C	TOC	Osi
237.8	0.8	2166.1	9.18	6.9444	0.0339	0.571	-27.98	5.6	0.191
167.5	0.6	1722.0	7.46	5.5328	0.0278	0.584	-28.05	5.5	0.182
68.3	0.3	1121.4	5.8	3.6622	0.0227	0.634	-28.53	4.0	0.195
123.0	0.5	992.8	4.6	3.3032	0.0187	0.575	-28.18	4.6	0.235
118.5	0.5	1216.2	5.6	4.0447	0.0220	0.594	-28.22	4.1	0.292
126.8	0.5	1194.8	5.4	3.8838	0.0207	0.590	-27.69	4.2	0.202
248.1	0.9	501.8	2.2	1.7753	0.0090	0.582	-27.92	4.2	0.232
214.4	0.8	916.6	4.0	2.9464	0.0148	0.581	-27.72	3.9	0.131
162.7	0.7	394.6	1.9	1.5538	0.0095	0.602	-27.89	3.8	0.344
170.3	0.8	463.1	2.7	1.6606	0.0106	0.617	-27.46	4.3	0.242
133.5	0.8	505.7	3.6	1.8065	0.0146	0.682	-27.52	3.6	0.258
154.1	0.8	401.2	2.5	1.5011	0.0109	0.597	-27.06	1.7	0.273
381.8	1.4	284.7	1.4	1.0598	0.0054	0.544	-26.78	4.1	0.189
149.3	0.9	450.3	3.1	1.5866	0.0126	0.667	-27.09	5.2	0.210
327.2	0.9	472.7	2.0	1.6746	0.0058	0.476	-26.84	4.9	0.230
318.2	0.7	498.5	2.0	1.7729	0.0056	0.400	-26.94	4.9	0.250
286.4	1.0	387.8	1.9	1.4600	0.0073	0.514	-27.05	5.5	0.275
65.7	0.6	296.4	2.8	1.4801	0.0178	0.688	-30.49	3.8	0.575
66.9	0.5	259.0	2.3	1.3023	0.0149	0.654	-30.54	5.2	0.511
80.0	0.8	431.7	4.4	1.9340	0.0242	0.715	-30.14	2.9	0.616
93.9	0.6	272.5	2.0	1.4359	0.0123	0.648	-30.83	4.8	0.604
58.7	0.5	161.9	1.4	1.1121	0.0127	0.651	-30.37	4.1	0.618
47.4	0.5	393.2	4.0	1.8589	0.0232	0.716	-29.40	2.5	0.659
39.8	0.4	451.4	4.9	1.9668	0.0255	0.730	-29.13	2.6	0.589
37.5	0.3	204.7	1.9	1.2283	0.0146	0.675	-28.85	2.9	0.604
40.5	0.4	473.0	5.1	1.9584	0.0252	0.723	-28.70	3.2	0.515
39.1	0.4	404.4	4.4	1.7781	0.0232	0.734	-28.33	3.4	0.544
36.6	0.3	628.4	6.0	2.4928	0.0264	0.770	-28.12	3.6	0.575
137.4	0.6	1200.1	6.5	4.0467	0.0200	0.686	-27.12	3.3	0.387
90.9	0.6	1282.1	8.9	4.3061	0.0295	0.788	-27.41	3.0	0.399
94.2	0.5	1528.1	10.1	5.1050	0.0312	0.781	-27.29	3.1	0.449
83.8	0.6	1295.9	9.7	4.3570	0.0331	0.793	-27.13	2.0	0.409
110.5	0.6	876.6	5.6	3.0276	0.0208	0.686	-27.24	3.1	0.357
147.4	0.6	1155.1	6.0	3.8489	0.0183	0.667	-27.41	4.2	0.331

±	Al (Wt %)	Ti (Wt %)
0.063	1.66	0.08
0.051	1.35	0.06
0.041	0.78	0.04
0.033	2.64	0.13
0.039	1.60	0.08
0.037	1.26	0.07
0.016	1.51	0.07
0.027	2.10	0.08
0.015	2.89	0.13
0.019		
0.026	1.06	0.06
0.019	1.95	0.11
0.010	0.97	0.06
0.022	1.02	0.06
0.012	1.46	0.08
0.012	2.61	0.16
0.013	5.22	0.31
0.026	4.11	0.21
0.022	4.60	0.24
0.038		
0.018	6.74	0.32
0.017	6.77	0.37
0.035	4.92	0.29
0.040	4.33	0.25
0.020	6.34	0.34
0.041	6.64	0.38
0.037	3.77	0.20
0.045	3.76	0.15
0.040	4.45	0.22
0.057	4.89	0.27
0.062	8.11	0.48
0.063	9.88	0.50
0.038		
0.037	6.28	0.37

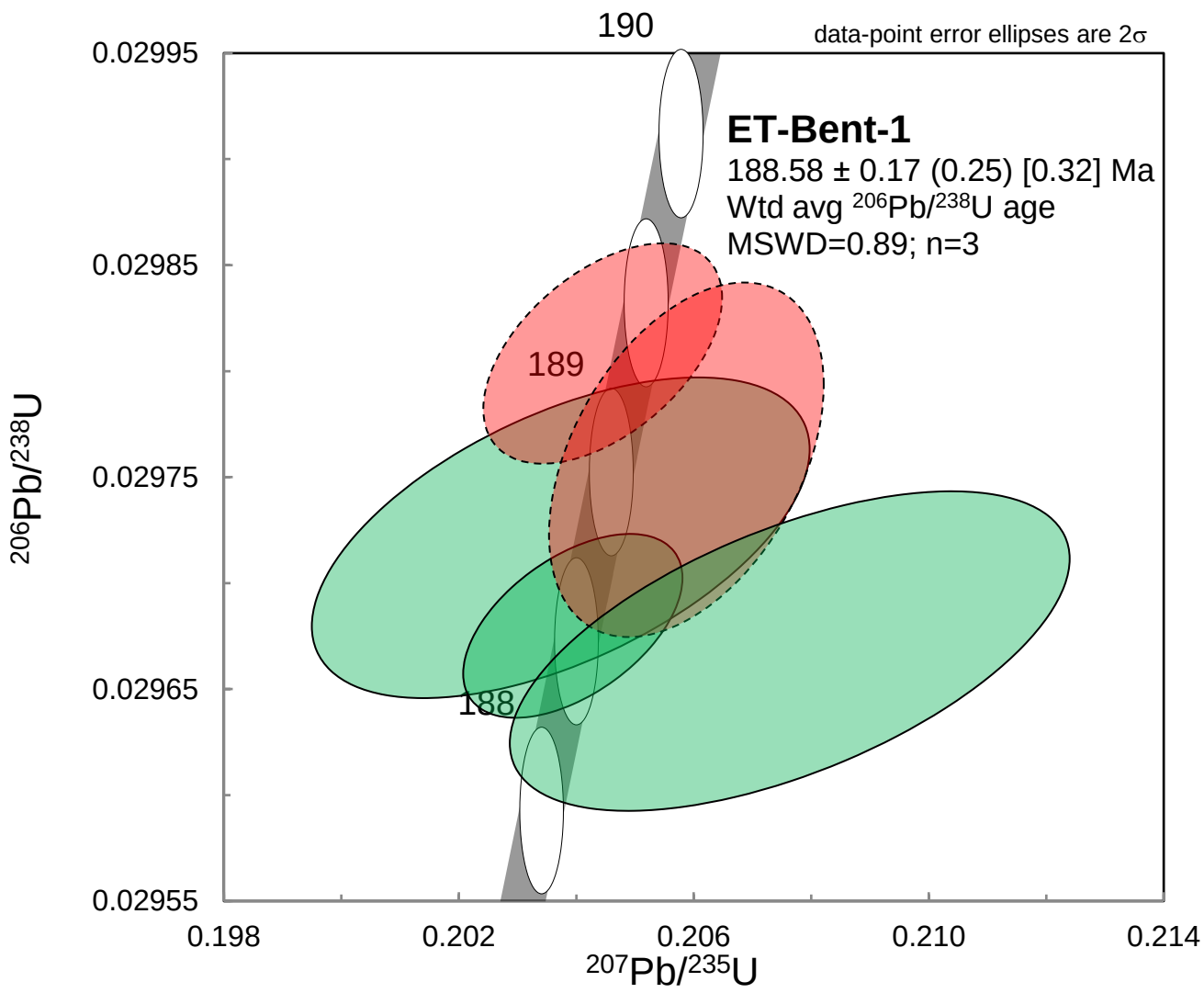
190
data-point error ellipses are 2σ
ET-Bent-1
188.58 ± 0.17 (0.25) [0.32] Ma
Wtd avg 206Pb/238U age
MSWD=0.89; n=3
189
188
0.02995
0.02985
0.02975
0.02965
0.02955
206Pb/238U
0.198
0.202
0.206
0.210
0.214
207Pb/235U

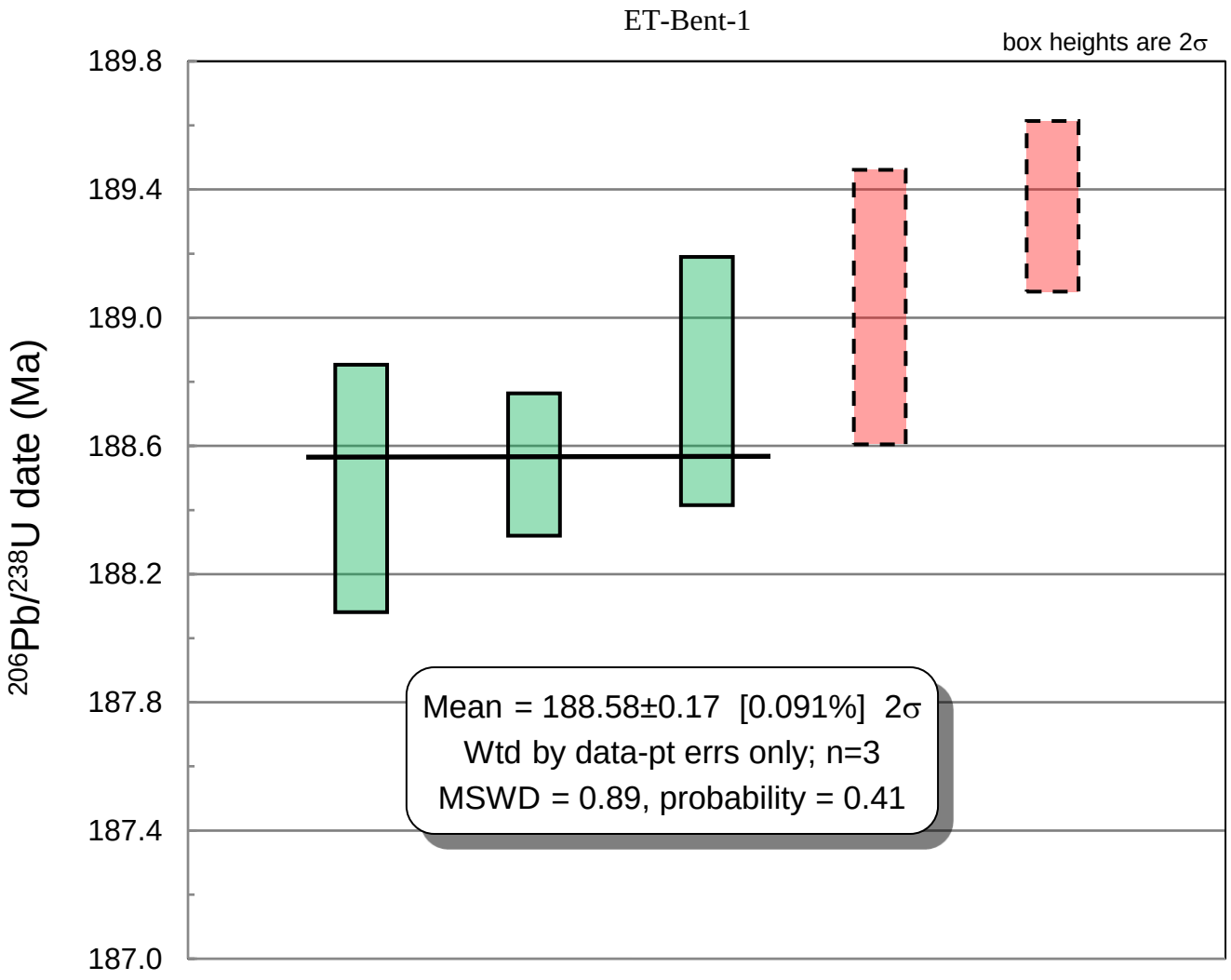
ET-Bent-1
box heights are 2σ
189.8
189.4
189.0
188.6
188.2
187.8
187.4
187.0
206Pb/238U date (Ma)
Mean = 188.58±0.17 [0.091%] 2σ
Wtd by data-pt errs only; n=3
MSWD = 0.89, probability = 0.41

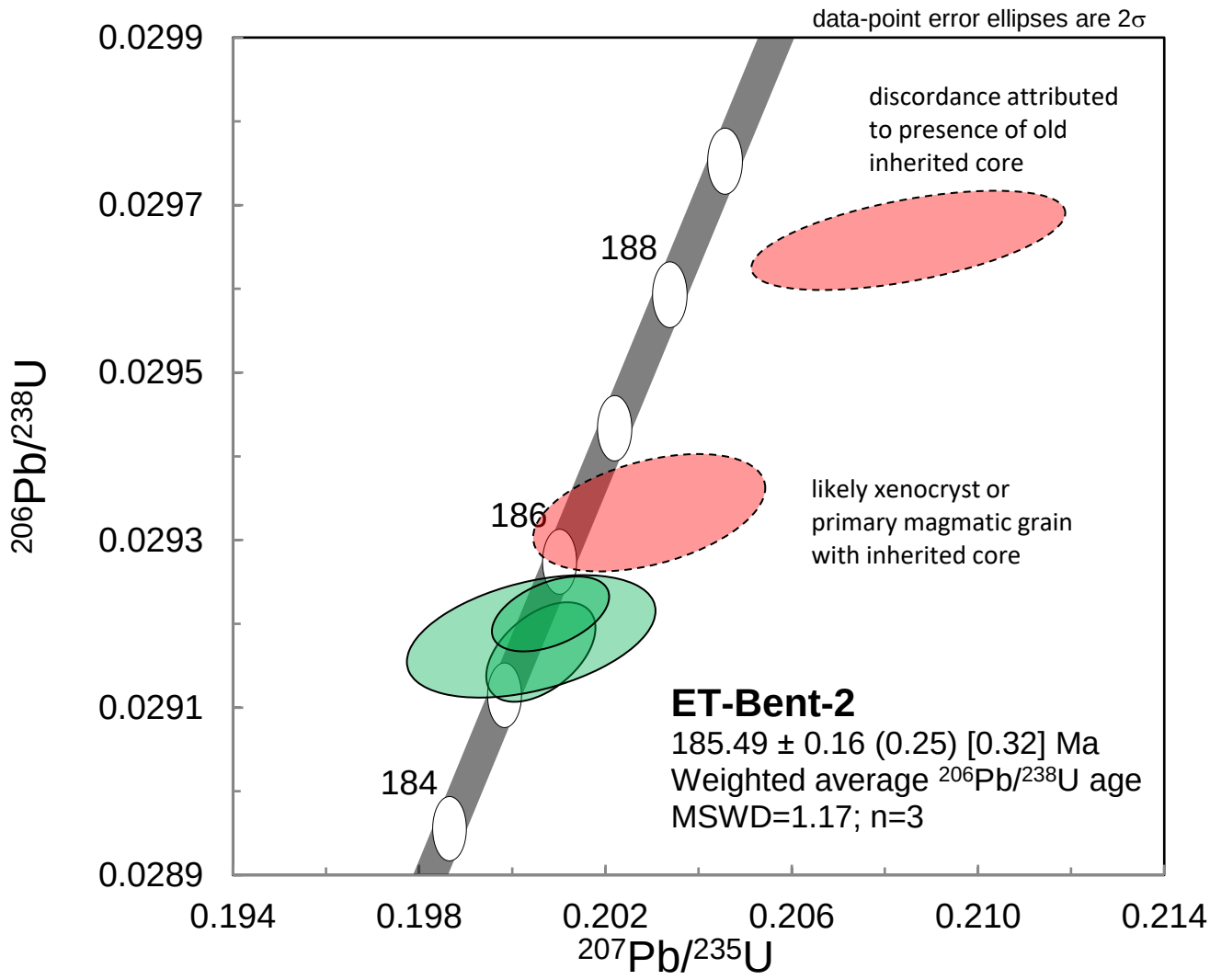
data-point error ellipses are 2σ
discordance attributed to presence of old inherited core
likely xenocryst or primary magmatic grain with inherited core
188
186
184
ET-Bent-2
185.49 ± 0.16 (0.25) [0.32] Ma
Weighted average 206Pb/238U age
MSWD=1.17; n=3
0.0299
0.0297
0.0295
0.0293
0.0291
0.0289
206Pb/238U
0.194
0.198
0.202
0.206
0.210
0.214
207Pb/235U

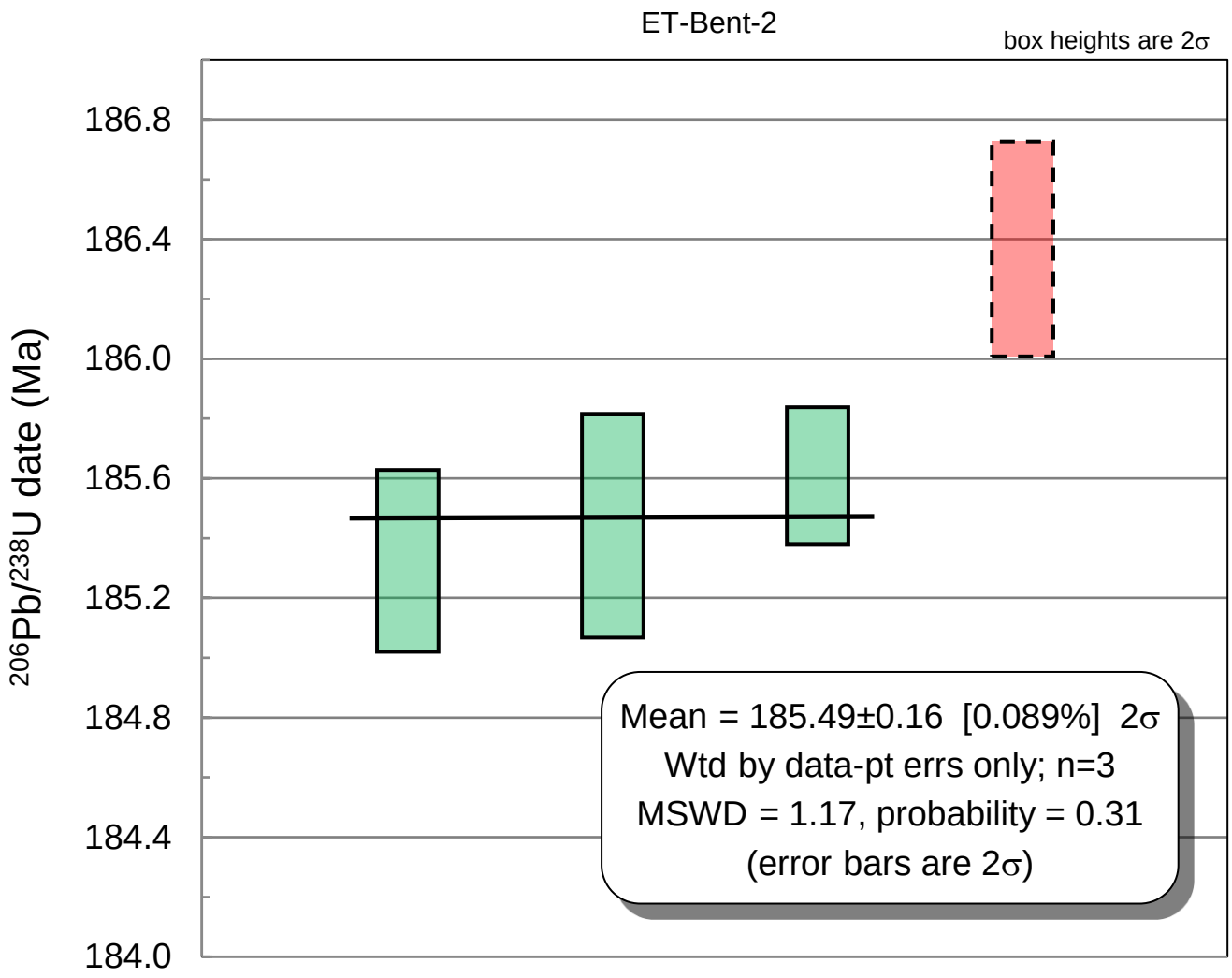
ET-Bent-2
box heights are 2σ
$^{206}Pb/^{238}U$ date (Ma)
186.8
186.4
186.0
185.6
185.2
184.8
184.4
184.0
Mean = 185.49±0.16 [0.089%] 2σ
Wtd by data-pt errs only; n=3
MSWD = 1.17, probability = 0.31
(error bars are 2σ)

U-Th-Pb isotopic data

		Compositional Parameters								Radiogenic Isotope Ratios								Isotopic Ages					
Sample	Wt. mg	U ppm	Pb ppm	Th/U	$^{206}Pb^*$ x10^{-13} mol	mol % $^{206}Pb^*$	Pb^*/Pb_c	Pb_c (pg)	$^{206}Pb/^{204}Pb$	$^{208}Pb/^{206}Pb$	$^{207}Pb/^{206}Pb$	% err	$^{207}Pb/^{235}U$	% err	$^{206}Pb/^{238}U$	% err	corr. coef.	$^{207}Pb/^{206}Pb$	±	$^{207}Pb/^{235}U$	±	$^{206}Pb/^{238}U$	±
(a)	(b)	(c)	(c)	(d)	(e)	(e)	(e)	(e)	(f)	(g)	(g)	(h)	(g)	(h)	(g)	(h)		(i)	(h)	(i)	(h)	(i)	(h)
ET-Bent-1																							
A	0.0069	51	1.7	0.525	0.4356	96.96%	10	1.12	608	0.167	0.04971	1.593	0.2037	1.699	0.02972	0.208	0.552	182	37	188.3	2.9	188.81	0.39
B	0.0024	322	10.4	0.443	0.9467	98.22%	17	1.41	1041	0.141	0.04974	0.750	0.2044	0.812	0.02981	0.143	0.505	183	17	188.9	1.4	189.35	0.27
C	0.0040	206	6.6	0.496	1.0120	98.66%	22	1.13	1385	0.158	0.04983	0.693	0.2039	0.747	0.02968	0.119	0.521	187	16	188.4	1.3	188.55	0.22
D	0.0066	146	4.7	0.514	1.2020	98.99%	30	1.00	1840	0.165	0.05017	0.857	0.2059	0.928	0.02976	0.230	0.421	203	20	190.1	1.6	189.04	0.43
E	0.0021	233	8.2	0.553	0.6008	96.38%	8	1.86	511	0.179	0.05076	1.763	0.2076	1.874	0.02967	0.208	0.578	230	41	191.6	3.3	188.47	0.39
ET-Bent-2																							
A	0.0043	391	11.9	0.464	2.0289	99.72%	106	0.47	6543	0.148	0.04989	0.423	0.2006	0.478	0.02917	0.167	0.485	190	10	185.7	0.8	185.32	0.30
B	0.0017	447	13.5	0.396	0.9119	99.49%	58	0.38	3648	0.127	0.05018	0.938	0.2030	1.004	0.02933	0.196	0.423	203	22	187.6	1.7	186.37	0.36
C	0.0016	343	11.0	0.502	0.6631	98.83%	26	0.64	1587	0.163	0.05099	1.238	0.2085	1.321	0.02966	0.164	0.552	241	29	192.3	2.3	188.41	0.30
D	0.0007	995	31.0	0.497	0.8948	99.21%	38	0.59	2337	0.158	0.04981	1.020	0.2004	1.089	0.02918	0.205	0.416	186	24	185.5	1.8	185.44	0.37
E	0.0021	350	11.2	0.610	0.9098	99.45%	57	0.41	3389	0.194	0.04987	0.468	0.2008	0.512	0.02921	0.125	0.462	189	11	185.8	0.9	185.61	0.23

(a) A, B etc. are labels for fractions composed of single zircon grains or fragments; all fractions annealed and chemically abraded after Mattinson (2005) and Scoates and Friedman (2008).

(b) Nominal fraction weights estimated from photomicrographic grain dimensions, adjusted for partial dissolution during chemical abrasion.

(c) Nominal U and total Pb concentrations subject to uncertainty in photomicrographic estimation of weight and partial dissolution during chemical abrasion.

(d) Model Th/U ratio calculated from radiogenic $^{208}Pb/^{206}Pb$ ratio and $^{207}Pb/^{235}U$ age.

(e) Pb* and Pbc represent radiogenic and common Pb, respectively; mol % $^{206}Pb^*$ with respect to radiogenic, blank and initial common Pb.

(f) Measured ratio corrected for spike and fractionation only. Mass discrimination of 0.25±0.03%/amu based on analysis of NBS-982; all Daly analyses.

(g) Corrected for fractionation, spike, and common Pb; all common Pb was assumed to be procedural blank: $^{206}Pb/^{204}Pb$ = 18.50±1.0%; $^{207}Pb/^{204}Pb$ = 15.50±1.0%; $^{208}Pb/^{204}Pb$ = 38.40±1.0% (1σ errors).

(h) Errors are 2-sigma, propagated using the algorithms of Schmitz and Schoene (2007) and Crowley et al. (2007).

(i) Calculations are based on the decay constants of Jaffey et al. (1971). $^{206}Pb/^{238}U$ and $^{207}Pb/^{206}Pb$ ages corrected for initial disequilibrium in $^{230}Th/^{238}U$ using Th/U [magma] = 3.

ET-Bent-2

ET-Bent-1